Low relative-submergence effects in a rough-bed open-channel flow

MAXIME ROUZES ⓘ (IAHR Member), *Postdoctoral Researcher, Institut de Mécanique des Fluides de Toulouse (IMFT), Université de Toulouse, CNRS, Toulouse, France*

FRÉDÉRIC YANN MOULIN ⓘ, *Assistant Professor, Institut de Mécanique des Fluides de Toulouse (IMFT), Université de Toulouse, CNRS, Toulouse, France*

EMMA FLORENS, *Postdoctoral Researcher, Institut de Mécanique des Fluides de Toulouse (IMFT), Université de Toulouse, CNRS, Toulouse, France*

OLIVIER EIFF ⓘ (IAHR Member), *Professor, Institute for Hydromechanics, Karlsruhe Institute of Technology, Karlsruhe, Germany*
Email: *olivier.eiff@kit.edu (author for correspondence)*

ABSTRACT
Multi-plane stereoscopic PIV measurements were performed in an open-channel flume fitted with cubes to investigate very low submergence ratios, $h/k = \{1.5, 2, 3\}$, where h is the water depth and k the roughness height. The spatial standard deviation of the mean flow components reveals that the extent of the roughness sublayer increases drastically with the decrease in h/k to span the entire water column for the lowest h/k investigated. Despite this, the logarithmic law is still observed on the double-averaged velocity profiles for all h/k, first with a fixed von Kármán constant κ and, second, via the indicator function where κ is a free parameter. Also, the longitudinal and vertical normal stresses indicate a universal boundary layer behaviour independent of h/k. The results suggest that the logarithmic and wake-defect laws can still be applied at such low h/k. However, the lateral normal stress depends on h/k in the range investigated as well as on the geometry of the roughness pattern.

Keywords: Double-averaging; logarithmic law; rough-wall boundary-layers; roughness sublayer; stereoscopic PIV; turbulent open-channel flows; relative submergence

1 Introduction

To model resistance effects due to the bed roughness in rivers and stream flows, flow resistance coefficients (Chezy, Manning–Strickler, Darcy–Weisbach) are usually used. These coefficients can be linked to boundary-layer theory characterized by a universal logarithmic function. In addition to high Reynolds numbers, an intrinsic condition in this theory is that the roughness elements' protrusion is small with respect to the boundary-layer depth. However, during floods with flows over the flood plains covered with vegetation and other structures, these roughness elements can become a macro roughness relative to the flow depth taken to be the boundary-layer depth. A similar situation might arise during low-water periods in lowland river beds or in mountainous rivers with larger gravel and rocks. Such low submergence situations put into question the applicability of boundary-layer theory to model and determine the

resistance coefficients. Katul, Wiberg, Albertson, and Hornberger (2002) suggest that flow resistance formulations based on the logarithmic law may fail for relative submergence ratios h/k below 10 (where h is the water depth and k is the roughness element height). Indeed, Bathurst (1985) found that Darcy–Weisbach friction-factor estimations in gravel-bed mountainous rivers for submergence ratios below 10 generally increase relative to the logarithmic-law formulations of Hey (1979). Similarly, the systematic evaluation by Rickenmann and Recking (2011) of various resistance formulations including common logarithmic ones with numerous field data concluded that the formulations should be used "with caution" for $h/D_{84} < 10$ (and the Manning–Strickler equation may be "unsuitable"). Laboratory open-channel studies to examine low-submergence effects for $h/k < 10$ with local measurements are scant and do not agree on the existence, applicability and evaluation method of the logarithmic law and its parameters

(e.g. Cooper, Aberle, Koll, & Tait, 2013; Franca, Ferreira, & Lemmin, 2008; Kironoto & Graf, 1994; Koll, 2006; Pokrajac, Campbell, Nikora, Manes, & McEwan, 2007). In the case of very low submergence, say $h/k < 3$, local studies are even rarer. One example is the study of Bayazit (1976) who concludes that the logarithmic law fitted over the entire water depth exists, but that the von Kármán constant decreases for $h/k < 3$. The underlying question to what extent the outer-law including the logarithmic layer and their parameters remain valid is still open. Part of the ambiguity appears to be due to a lack of detailed mean and turbulent local flow measurements and different methods of evaluation.

Since the seminal works of Nikuradse (1933) (translated into English in Nikuradse, 1950) on circular pipes and Keulegan (1938) on open channels, it is well known that increasing the bed roughness shifts and decreases the mean logarithmic velocity profile. The shift is generally taken into account by introducing into the logarithmic law either a roughness function ΔU^+, a roughness length z_0 or an equivalent-sand-roughness scale k_s. All representations yield a modified logarithmic law compared to the smooth turbulent flow case with interchangeable roughness parameters and associated roughness Reynolds numbers: ΔU^+, $z_o^+ = z_o u_*/\nu$ or $k_s^+ = k_s u_*/\nu$. However, with increasing roughness heights, the logarithmic law is not found to fit the data well and a shift in the origin of the vertical coordinate is introduced via a displacement height d (e.g. Jackson, 1981). Yet, perhaps because it is physically small, this crucial parameter is often determined in an ad hoc fashion, if at all. A consistent method to evaluate it was proposed by Nikora, Koll, McLean, Dittrich, and Aberle (2002). The logarithmic law with k_s and d writes:

$$\frac{\langle \bar{u} \rangle}{u_*} = \frac{1}{\kappa} \ln \left(\frac{z - d}{k_s} \right) + B_r \qquad (1)$$

where κ is the von Kármán constant and B_r is a constant for fully rough flows ($k_s^+ > 70$). Using the average diameters of glued sand grains for k_s, Nikuradse (1933) found B_r to be equal to 8.48, a value still widely used (e.g. Jiménez, 2004) to determine k_s for non-sand surfaces. In open-channels on glued-sand and gravel beds with $h/k_s = 10$ and using $k_s = D_{50}$, Kironoto and Graf (1994) show that $B_r = 8.47 \pm 0.9$, in accordance with Nikuradse's definition of k_s. Importantly, k_s is not a geometric but rather a hydraulic parameter (e.g. Jiménez, 2004). For gravel-bed rivers, Keulegan's (1938) form of the logarithmic law without the displacement height has been widely used to model the flow resistance coefficient (usually Darcy–Weisbach) based on the cross-sectionally averaged velocity by integrating it vertically across the water-depth. Better fits of the field measurements are obtained by setting k_s to a multiple of D_{84}, with suggested values in the range 2.2 to 3.5 (Ferguson, 2007). This factor effectively lowers the offset coefficient.

The outer layer, which includes most of the logarithmic layer, is not affected by the wall roughness according to Townsend's wall-similarity hypothesis (Townsend, 1980). The reviews of Raupach, Antonia, and Rajagopalan (1991) and Jiménez (2004) for canonical rough-wall boundary layers lend support to this hypothesis. However, wall similarity implies in addition to sufficiently high Reynolds numbers a clear scale separation between the roughness length-scale and the boundary-layer thickness (Jiménez, 2004). It is the scale-separation assumption which can be expected to break down in open-channel flows when the relative submergence ratio h/k decreases. Assuming that the full extent of the roughness sublayer (based on older estimates) directly affects the logarithmic layer and that at least half of the logarithmic layer should remain to maintain wall-similarity, Jiménez (2004) concludes that δ/k should be greater than at least 40, where δ is the boundary-layer depth. For $\delta/k < 40$, roughness-layer effects are estimated to significantly affect the outer layer so that outer-layer similarity is expected to break down. For fully-rough flows, this implies $\delta^+ > 4000$ for similarity to hold.

However, recent experimental studies on rough-wall boundary layers report that wall-similarity is still found for δ/k ratios below the threshold of Jiménez (2004). Flack and Schultz (2014) conducted experiments in a re-circulating water tunnel over sandpaper and mesh with scale ratios $16 < \delta/k < 106$ and observed similarity both in the mean velocity profile and the Reynolds stresses for all ratios investigated. This is consistent with Flack, Schultz, and Connelly (2007) who have shown similarity of both first and second-order turbulence statistics for $\delta/k > 19$. Comparing a set of developing rough-walled atmospheric-type zero-pressure-gradient boundary layers, Castro (2007) observed mean flow similarity even at the smallest measured fetch where δ/k is as low as 5. The similarity at this low ratio is judged to be borderline and the author speculates that for even lower ratios the buffer-layer approach is probably more appropriate. Amir and Castro (2011) investigated three roughness types, again for developing atmospheric-type zero-pressure-gradient boundary layers with a span of $2.5 < \delta/k < 25$ and compared to smooth wall data. They conclude that smooth and rough wall-bounded turbulent flows are completely indistinguishable for $\delta/k > 6$. For lower ratios, the Reynolds-stress profiles differ from their smooth-wall counterparts and the mean flow is judged to be noticeably affected by $\delta/k = 3$. Re-analysing these data and others with the diagnostic plot of Alfredsson, Segalini, and Örlü (2011) and Castro, Segalini, and Alfredsson (2013) show that the turbulent intensity in the outer layer plotted versus the relative mean flow collapses for fully-rough zero-pressure-gradient (ZPG) boundary layers (but not with the smooth-walled or transitional cases). Rather then use δ/k as the scale-separation parameter with a geometrical scale, the authors propose to use δ/z_0 with the roughness length, citing a critical value δ/z_0 of about 300, equivalent to $\delta/k_s \approx 9$. However, the available data in the diagnostic plot suggests collapse for even lower δ/z_0 values, in agreement with the Amir and Castro (2011) interpretation.

The existence of the logarithmic law and the universality of its constants is a matter of debate for canonical wall flows even at high submergence (high δ/k) for smooth walls. Nagib and Chauhan (2008), examining DNS and experimental data of pipe, channel and ZPG boundary-layer flows, show that the von Kármán constant for the Superpipe (pipe facility for very high Reynolds numbers) at 0.41 is higher than for the channel and ZPG boundary-layer value around 0.38 (at high enough Reynolds numbers). However, Marusic, Monty, Hultmark, and Smits (2013), also examining high Reynolds number experimental data for boundary layers, pipe flow and atmospheric surface layers (transitionally rough) conclude that within experimental uncertainty, a von Kármán constant of 0.39 describes all the tested data. In addition to possibly too low Reynolds numbers, part of the disagreement is due to the uncertainty in the determination of the friction velocity, the definition of the upper and lower bounds, and the wall-positioning sensitivity of the velocity measurements (Segalini, Örlü, & Alfredsson, 2013; Vinuesa, Schlatter, & Nagib, 2014).

In rough-bed open-channel flows, Bayazit (1976) found a logarithmic law over hemispheres with a von Kármán constant $\kappa = 0.41$ for $h/k > 3$ but with decreasing values for $h/k < 3$. This is in agreement with Kironoto and Graf (1994) who confirmed a logarithmic law with $\kappa = 0.41$ for $6 < R_h/k_s < 20$ (R_h is the hydraulic radius). Other studies, however, found lower values of κ even for the intermediate range $3 < h/k < 10$, such as Koll (2006) for $3 \lesssim h/k \lesssim 12$, Franca et al. (2008) for $h/D_{50} = 5.25$ and 5.96 and Mohajeri, Grizzi, Righetti, Romano, and Nikora (2015) for $7.5 < h/k < 10.8$. For lower submergence ratios, Manes, Pokrajac, and McEwan (2007) found κ values around 0.3 for $h/k = 2.3$ and 4 and consider this as evidence that the logarithmic law is not applicable (Nikora, Goring, McEwan, & Griffiths, 2001), while for $h/k = 6.5$, they find support for the logarithmic law with $\kappa = 0.4$. Pokrajac et al. (2007), examining open-channel flow over 2D bars, argue that if the roughness sublayer extends up to the $0.15h$–$0.2h$, the velocity profile may still be logarithmic but its parameters "may not have the same physical meaning as the parameters of universal log law". For $h/k = 15.8$, they conclude the logarithmic law exists even though they find $\kappa = 0.55$, higher than 0.4. Thus, although far from a general agreement, there is an explicit or implicit suggestion that if κ differs too much from its universal value for low submergence, the logarithmic law may not be applicable. Yet, even for canonical high-submergence wall flows, the debate on whether κ is universal or depends on the flow is still open.

One issue in the necessary scale separation for similarity to hold is the actual height of the roughness sublayer which is thought to directly affect the logarithmic layer. As shown by Florens, Eiff, and Moulin (2013) for open-channel flow over a bed of cubes in a square arrangement, the determination of the roughness sublayer height needs extensive measurements and careful analysis to remove biases due to spatial and temporal convergence errors. As a consequence, the height of the roughness sublayer appears to have generally been overestimated, which leads to more conservative estimations for the necessary scale separation. The roughness sublayer heights found by Florens et al. (2013) are in the range $1.1k$–$1.2k$ with a 5% threshold level, well below the usual heights cited in the literature: 2–$5k$ Raupach et al. (1991); 2–$5k$ Jiménez (2004); 3–$5k_s$ Flack, Schultz, and Shapiro (2005); or 2–$5k$ Nikora et al. (2001). Nikora et al. (2001), examining open-channel flows, use the estimation of Raupach et al. (1991) to define and delineate different flow types, in particular a flow type II with $1 > h/k > (2 - 5)$ for which no logarithmic law is presumed to exist (Nikora, Koll, McEwan, McLean, & Dittrich, 2004). However, in the flow over the same bed as in Florens et al. (2013) as well as over a staggered cube arrangement, Eiff, Florens, and Moulin (2014) found logarithmic laws for h/k down to the lowest investigated ratio of 3 – with $\kappa = 0.41$. Moreover, the logarithmic law, based on the double-averaged longitudinal velocity, was found to penetrate the roughness sublayer, in agreement with the view of Castro (2007). In this view, the roughness sublayer acts more like the rough-wall equivalent of the inner layer (Florens et al., 2013) rather than a buffer layer as suggested by Jiménez (2004). This suggests that the logarithmic layer could be observed for even lower submergence values and still be appropriate to model the roughness parameters and flow resistance. However, consistent measurements including a roughness sublayer characterization as well as first and second-order turbulence statistics at submergence values h/k lower than 3 have not been examined yet, likely because measurements in the thin layer of water above the roughness elements are challenging by any method.

Here we propose a systematic investigation of very low relative submergence with $h/k = \{1.5, 2, 3\}$ for open-channel flow over a bed of cubes in a square arrangement. The three velocity components were measured in three planes across one roughness pattern with a stereoscopic PIV technique. By using a channel made of glass in combination with transparent cubes through which the laser sheet can penetrate from below, spatially-averaged quantities of first-, second- and third-order turbulence statistics were obtained without the need to perturb the free surface (for example by the use of a glass plate). Not to perturb the free surface is particularly crucial here due to the very shallow flows investigated. The experimental set-up for the flow generation and the optical measurements are presented in Section 2. The main features of the three-dimensional mean flow are discussed in Section 3. The roughness sublayer structure is presented and discussed in Section 4. In Section 5, the logarithmic and outer laws and its parameters will be sought by different methods, including the Clauser method with a fixed $\kappa = 0.41$ and a free-κ method based on the indicator function (Mohajeri et al., 2015; Segalini et al., 2013; Spalart, 1988). The existence and universality of these laws will also be discussed in Section 5 using evaluations of the mixing length and turbulence statistics. Final conclusions are drawn in Section 6.

2 Experimental set-up

2.1 Flow generation

Experiments were carried out in a 26 m long, 1.10 m wide and 0.50 m deep open-channel flume, with a slope of 0.3% and a 13.20 m long working section made out of glass (Fig. 1). The flume is located within the Environmental Fluid Mechanics facility of the Institut de Mécanique des Fluides de Toulouse (IMFT). The water discharge ranges from 1 L s^{-1} up to 150 L s^{-1}, measured by electromagnetic flow metres with an accuracy of $\pm 0.2\%$. The flume works in a closed loop: the water is pumped from the downstream water tank and transported through pipes upstream into a 5 m long tranquillizing entry section. To establish a uniform flow and to reduce both surface waves and the background turbulence intensity, the flow in the entry section passes through a honeycomb and a series of perforated plates before converging at the main channel entrance.

The channel's glass bottom was fitted with a rough bed composed of cubes between $x = 2.60$ m and $x = 24$ m, where x is the longitudinal coordinate, the origin being defined at the end of the entry section (Fig. 1). The measurement area is located at $x_M = 19.20$ m. The set-up limits the growth of the incoming smooth boundary layer to a thickness lower than the roughness height k to avoid an internal boundary-layer growth. The subsequent length of the flow over the roughness elements with flow depths of less than 6 cm assures that the flow is fully developed well before the measurement area (Florens, 2010). Also, the backwater curve generated by the downstream boundary condition is sufficiently weak to consider the flow uniform in the measurement area. Flow-depth measurements along the flume confirm that the degree of non-uniformity defined as the ratio of water depth $h(x)$ to the normal water depth h_n is below 1% in the measurement zone (Rouzes, 2015).

In the downstream direction, the right half of the channel was fitted with 2 cm cubes arranged in a square configuration with a frontal density (frontal area, A_f, to planar area, A_p) $\lambda_f = 0.20$, whereas the other half was arranged using the same roughness elements, but in a staggered configuration leading to a frontal density $\lambda_f = 0.40$. These rough beds are respectively noted S1 and S2 (Fig. 2a) and correspond to the beds used separately across the channel width in Eiff et al. (2014). The hybrid set-up was designed to also study the horizontal mixing layer and secondary currents generated around a bed roughness discontinuity of two homogeneous rough beds. With effective channel-halfwidth to water-depth aspect ratios as low as 14 (and up to 55), the flow in the centre of each roughness area is considered to be two-dimensional (see Nezu & Rodi, 1985) across a minimum of about 9 (and a maximum of 50) effective water depths taken here as the depth above the roughness elements. All measurements and analyses presented herein pertain to the centre of roughness area S1 (square, $\lambda_f = 0.20$). In accordance, the coordinate system is defined with respect to this roughness area, i.e. the origin of the coordinate system taken at the end of the entry section is at the bottom and centre of roughness area S1 (Figs 2a and 2b). The x, y and z-axes and associated velocity components u, v and w are defined respectively as the streamwise, lateral and vertical directions.

In all, three relative submergence ratios h/k equal to 1.5, 2 and 3 were studied (regimes E06, E04 and E03, respectively), whose control parameters and flow characteristics are given in Table 1.

2.2 Stereoscopic PIV measurements

Florens et al. (2013), using 2D PIV in longitudinal-vertical planes, analysed the sensitivity of both the temporal and spatial convergence on the statistics resulting from the
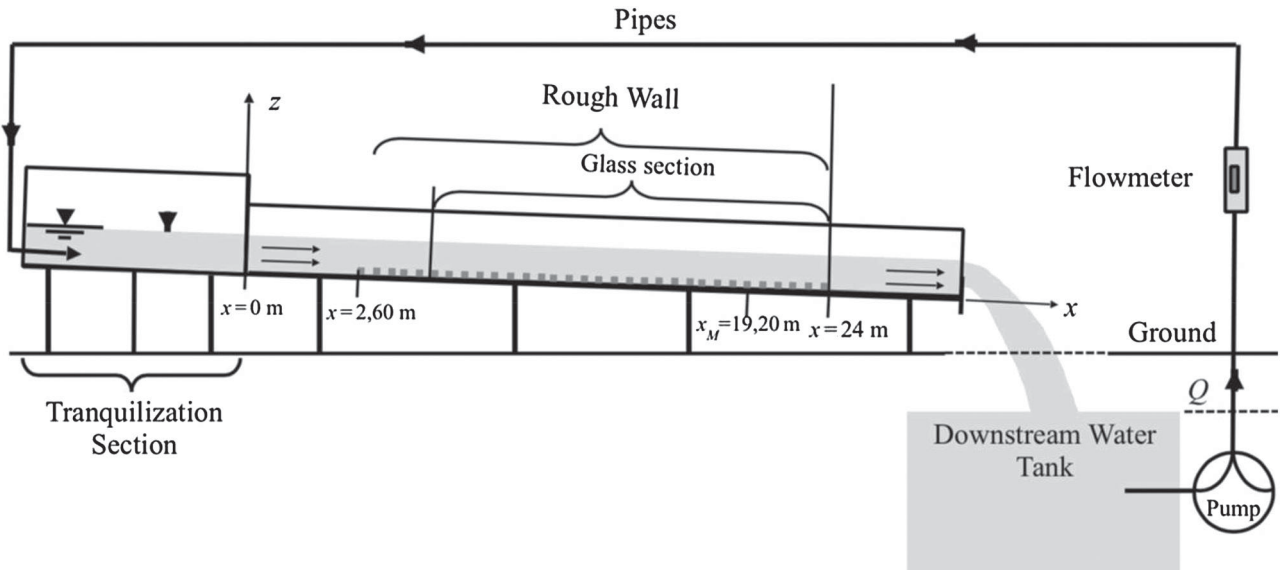

Figure 1 Sketch of the open-channel facility (not to scale). The rough bed is located between $x = 2.60$ m and $x = 24$ m, with the measurements performed at $x_M = 19.20$ m
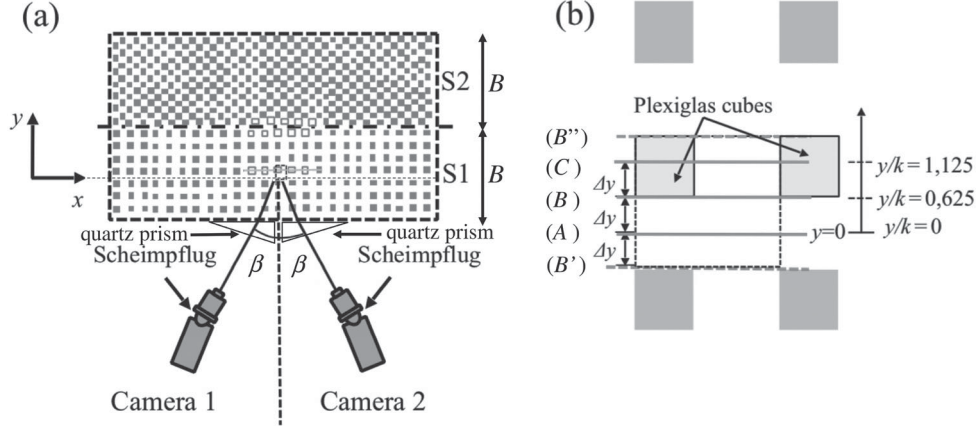
Figure 2 (a) Top view of the stereoscopic PIV set-up (not to scale). All measurements were performed in the centre of rough bed S1 (2 cm cubes in a squared configuration with frontal density $\lambda_f = 0.2$). (b) Position of the three measurement planes (A), (B) and (C) over the roughness pattern. By symmetry considerations, two virtual planes (B') and (B'') are defined over the roughness pattern and used for a five-plane double-averaging process

Table 1 All flow regimes investigated and their associated experimental parameters[a]

Regime	h (m)	h/k	Q (m^3 s^{-1})	U_d (m s^{-1})	Fr	u_* (m s^{-1})	k_s^+
E06	0.061	3	0.0159	0.352	0.55	0.0361	426
E04	0.041	2	0.0053	0.229	0.50	0.0247	146
E03	0.031	1.5	0.0022	0.181	0.55	0.0180	90

[a]h is the water depth, h/k the relative submergence ratio, Q the water discharge, U_d the bulk velocity over the whole width of the channel defined with an effective water depth $h - k$, $\mathrm{Fr} = U_d/(\sqrt{g(h-k)})$ the Froude number based upon the water flow above the roughness elements, u_* the friction velocity at $z = k$ inferred from the total shear stress profiles, and $k_s^+ = k_s \, u_*/\nu$ the roughness Reynolds number, where k_s is computed from the constant-κ method.

double-averaging methodology. They showed that even a relatively high number of temporally averaged vertical profiles across the roughness pattern (4 or 25), typically obtained via point measurements, was not sufficient to converge spatially, but that five PIV planes with 400 profiles converged within 1%. This of course still holds for stereoscopic PIV measurements which yield the out-of-plane velocity component in addition to the two components in the laser-sheet plane. The laser-sheet plane arrangement proposed by Florens et al. (2013) over the same rough bed as here offers the possibility to achieve spatially converged estimates by using only three equispaced laser-plane measurements over the periodic roughness pattern, $y/k = 0$: plane (A), $y/k = 0.625$: plane (B) and $y/k = 1.125$: plane (C) (Fig. 2b). As in Florens et al. (2013), the remaining two planes can be obtained by considering the lateral periodicity of the mean flow, in particular the mean flow in plane (B) whose mirror images are located at $y/k = -0.625$ and $y/k = 1.687$ (with a laser sheet thickness of 2.5 mm), respectively denoted plane (B') and plane (B'') and marked by dotted green lines in Fig. 2b). The two "virtual" planes are obtained directly from the velocity measurements in plane (B), except the lateral velocity component v which is multiplied by -1 due to the mirror symmetry.

The laser sheet is generated by a double-cavity pulsed 200 mJ Nd:Yag Laser (Quantel CFR200) emitting at 532 nm. The laser sheet enters the water column from below, as shown in Fig. 3. To generate the 2.5 mm thick and 15 cm wide collimated laser sheet in the measurement area, the laser beam first passes through a laser-sheet generator which creates the 2D laser sheet by first reducing the thickness of the laser beam with a convergent lens, and then expanding it into a laser sheet via a cylindrical divergent lens. The laser sheet then passes through a convergent lens located at the focal point, resulting in a collimated laser sheet, and is then reflected vertically by a 45° inclined mirror below the flume. In planes (A) and (B), the laser sheet passes through the glass bottom of the channel, whereas in plane (C), it also passes through the cubes made of transparent Plexiglas®. For the latter plane, the collimation of the laser sheet avoids large shadowing above the cubes' interfaces so that only very thin vertical shadows are left across which the correlations can be computed. This allows the velocity field to be computed across the entire extent of all planes.

The stereoscopic PIV images were recorded with two high-resolution (2560×2160 px^2) 14-bit sCMOS cameras (LaVision Edge) fitted with 105 mm Nikon lenses and LaVision Mount Version 3 Scheimpflug adapters. The cameras were symmetrically placed alongside the channel to view the flow through the glass walls fitted with 45° quartz prisms (Figs 2a and 3). The Scheimpflug adapters make the laser-sheet plane and the plane of focus coincide (Prasad & Jensen, 1995) while the prisms were used to diminish optical aberrations and to allow suitable camera angles (Calluaud & David, 2004). The cameras' angle β (defined in Fig. 2a) was set to about 32° to optimize the resolution of both the in-plane and out-of-plane velocity components. The flow was seeded with 10 µm hollow glass spheres with a
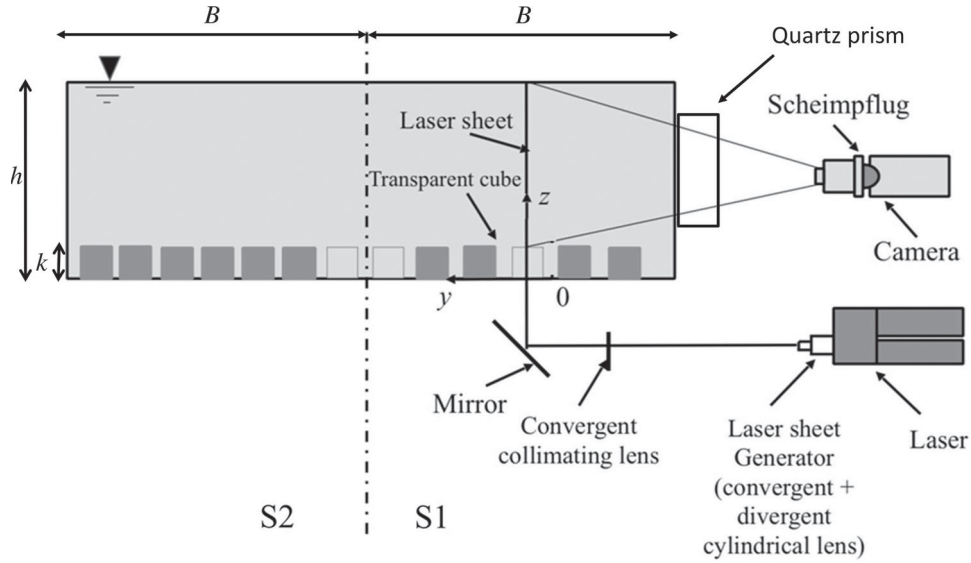
Figure 3   Downstream view of the experimental set-up with collimated laser-sheet generation and optical path

density of 1100 kg m^{-3} (Dantec, HGS-10). The beads were injected in the downstream water tank to be thoroughly homogeneous in the measurement zone. For each measurement plane, 3000 stereo image pairs were acquired at 3 Hz, a frequency chosen low enough to allow all 3000 velocity fields to be statistically independent for the computation of the mean and turbulence statistics. The statistical independence was confirmed by streamwise-velocity auto-correlation function computations for all planes and submergence ratios which revealed values below 0.1 at the lag time of the sampling interval.

For the stereo calibration, a two-level calibration plate was chosen (LaVision #106-10) and aligned with the vertical laser sheet. Using the Davis Flowmaster Stereo-PIV software, the acquired images were first dewarped into the laser plane, then the 2D2C-vector field was computed for each camera in the planar Cartesian grid. A self-calibration tool was used to correct the micro-metric misalignment between laser-sheet direction and two-level calibration plate. In-plane and out-plane velocity components were then computed from the velocity fields measured by the two cameras. All images were acquired in a coordinate system fixed and aligned with the inclined channel bottom (Fig. 1). Consequently, all velocity fields were projected in that coordinate system.

Before performing the PIV correlations, the images were pre-processed using a particle intensity normalization filter (min/max filter). The PIV-processed area is 10.5 cm wide and extends through the whole water column above the cubes with a uniform spacing (Δx, Δz) of 0.45 mm. The width corresponds to 2.5 roughness pattern wave-lengths. The PIV correlations were performed with an interrogation box size of 24×24 pixels (i.e. about 0.9×0.9 mm^2 in the flow), with an overlap of 50%. Considering the correlation box size as the smallest resolved length scale such as in Lavoie, Avallone, De Gregorio, Romano, and Antonia (2007) rather than the smaller grid spacing, the spatial resolution is about 15, 11 and 9 Kolmogorov length

scales for $h/k = \{1.5, 2, 3\}$, respectively, using the estimate of Coceal, Thomas, Castro, and Belcher (2006) for boundary layers.

Florens et al. (2013) had optical access within the canopy by using a special 2D PIV set-up. In the stereo configuration this is not possible. Also, just above the roughness elements, light reflections and absorption around the cubes' edges lead to a relatively poor image quality so that despite image pre-processing, the PIV algorithms yielded some false vectors in that thin region. The percentage of false vectors at $z/k = 1.1$ reaching 10%, 9% and 12.5% for $h/k = \{1.5, 2, 3\}$, respectively, only vectors for $z/k > 1.1$ were further analysed.

Double-averaged quantities were computed on a width equal to one roughness pattern at the centre of the measurement area. Over the five planes this yields $5 \times 96 = 480$ vertical velocity profiles in the streamwise direction with 8, 28 and 71 levels for $h/k = \{1.5, 2, 3\}$ respectively.

3   Mean flow and turbulence statistics

In this section, the effect of low relative-submergence ratios on the mean flow and turbulence statistics is examined. First, the time-averaged velocity fields for each of the three measured planes are examined (Section 3.1). Second, the single-plane double-averaged velocity profiles planes and the five-plane double-average (i.e. the roughness-pattern double-average) are discussed to elucidate the inter-plane spatial variance (Section 3.2). Third, the five-plane spatially-averaged turbulent stresses are examined (Section 3.3) and finally, the five-plane spatially-averaged skewness factor (Section 3.4).

3.1   Time-averaged velocity fields

The three time-averaged velocity fields ($\bar{u}, \bar{v}, \bar{w}$) are plotted in Figs 4–6, respectively, for each of the three measured vertical
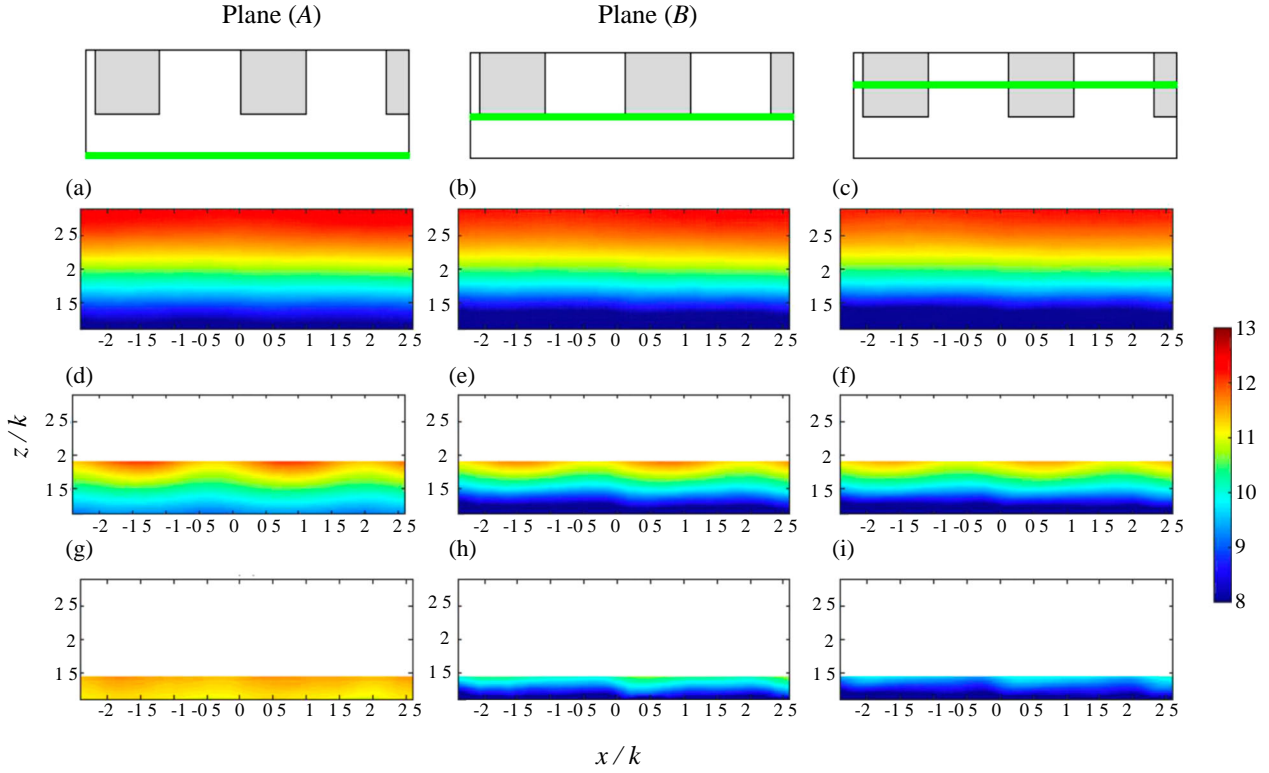
Figure 4   Time-averaged streamwise velocity fields $\bar{u}/u_*$ for measurement planes (A), (B) and (C). (a), (b) and (c): $h/k = 3$ (E06); (d), (e) and (f): $h/k = 2$ (E04); (g), (h) and (i): $h/k = 1.5$ (E03)
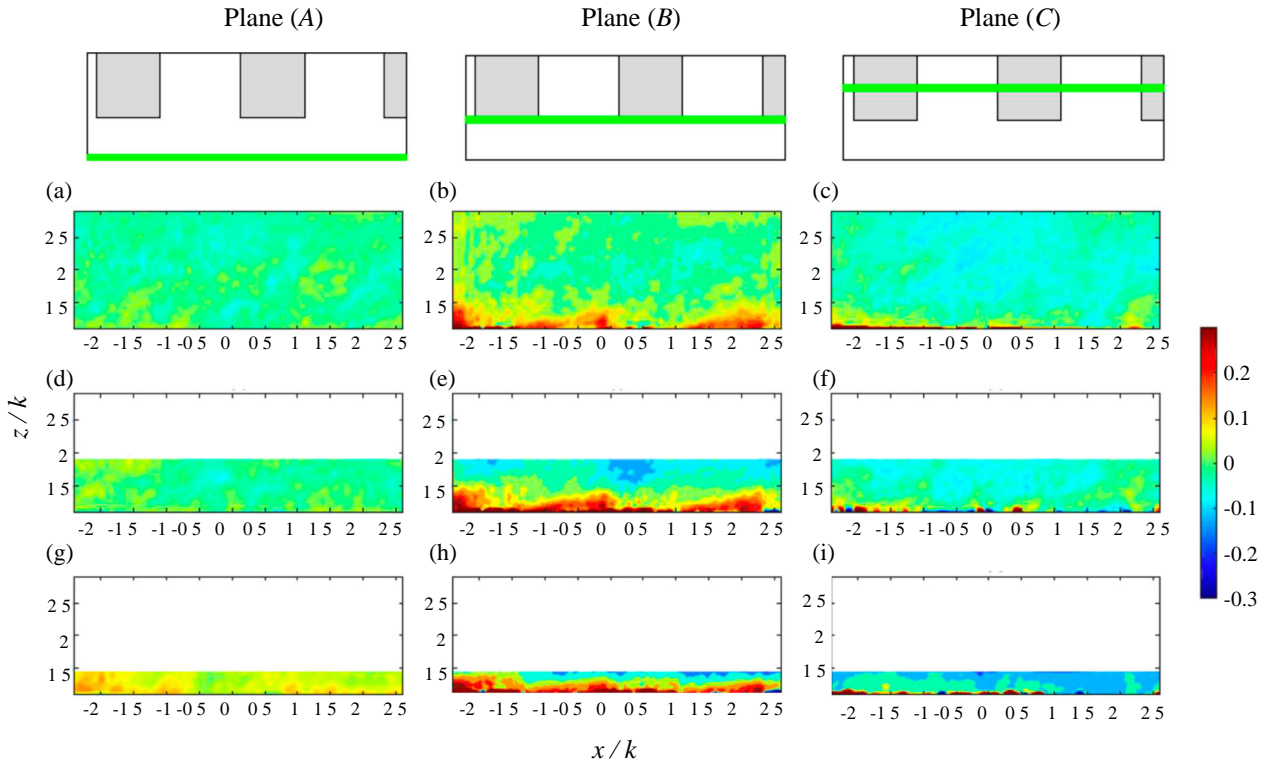
Figure 5   Time-averaged transverse velocity fields $\bar{v}/u_*$ for measurement planes (A), (B) and (C). (a), (b) and (c): $h/k = 3$ (E06); (d), (e) and (f): $h/k = 2$ (E04); (g), (h) and (i): $h/k = 1.5$ (E03)

planes (A,B,C) and each of the three submergence ratios $h/k = \{1.5, 2, 3\}$. All velocities are normalized by the friction velocity u_* (Table 1), as determined later in Section 3.3 (constant-κ method). It can be seen in Fig. 4a–c that $\bar{u}/u_*$ for $h/k = 3$ is essentially homogeneous in all three planes except near the canopy top, while this is not the case any more for the two

Figure 6   Time-averaged vertical velocity fields $\bar{w}/u_*$ for measurement planes (A), (B) and (C). (a), (b) and (c): $h/k = 3$ (E06); (d), (e) and (f): $h/k = 2$ (E04); (g), (h) and (i): $h/k = 1.5$ (E03)
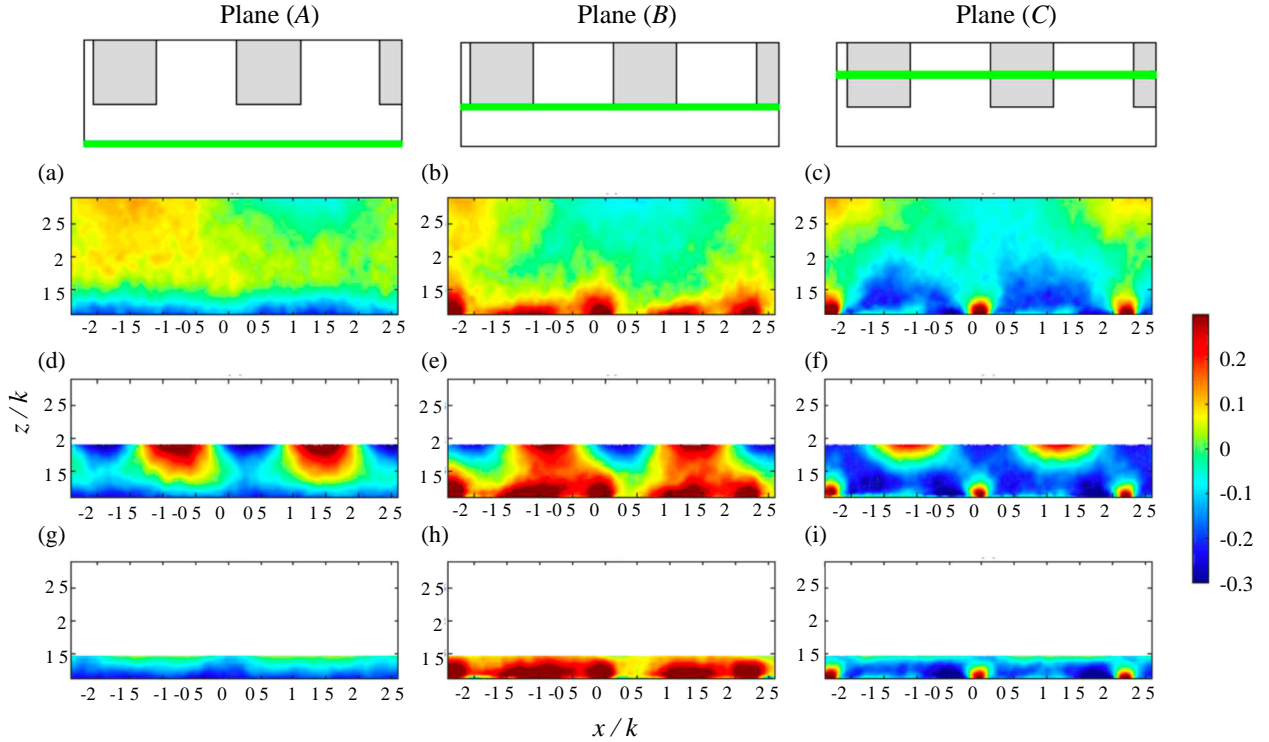
lower submergence ratios shown in Fig. 4d–f and 4g–i, respectively. The time-averaged vertical velocity fields $\bar{w}/u_*$ for the same flow regime ($h/k = 3$) shown in Fig. 6a–c for all three planes, on the other hand, are non-uniform throughout the water column. Closer to the canopy top, the time-averaged vertical velocity is marked by periodic patterns of low and high vertical velocities in planes (B) and (C) (Fig. 6b and 6c). As expected, high-velocity areas are located directly above the upstream edge of the cubes, and compensated by downward velocities above and behind the cubes in the centre plane (C). The time-averaged lateral velocity fields $\bar{v}/u_*$ plotted in Fig. 5a–c complete the picture. As expected from the roughness elements' symmetry, values close to zero are found everywhere, except in the vicinity of the cubes in the side plane (B), where positive values are found that compensate the upwards velocities of the centre and side planes, (C) and (B). Clearly, this mean flow structure, periodic with the same periodicity as the rough bed, marks the presence of the roughness sublayer which extends above the roughness elements. The spatial standard deviations (D_s) for the mean velocity components, presented later in Section 4.1, quantify the level of spatial inhomogeneity in this complex mean flow topology.

The time-averaged velocity fields for $h/k = 2$ of the streamwise, lateral and vertical components are plotted in Figs 4d–f, 5d–f and 6d–f, respectively. For this submergence regime, while the flow patterns close to the cubes are similar to the ones observed for $h/k = 3$, both the longitudinal and vertical velocity components exhibit high- and low-velocity areas

which occur periodically in the vicinity of the free surface. Those zones are in phase with the period of the roughness pattern. High-velocity areas for the streamwise velocity component (Fig. 4d–f) correspond to low-velocity areas for the vertical velocity component (Fig. 6d–f). Yet, such patterns near the free surface do not appear clearly in the fields of the mean lateral velocity (Fig. 5d–f). Also, it can be observed that near the free surface, the vertical-velocity patterns are decreasing with depth.

One may suspect that these strong periodic features for $h/k = 2$ are due to the presence of a stationary surface gravity-wave generated by resonance of the periodic roughness pattern (or the roughness sublayer flow pattern acting as a virtual-bottom boundary condition). The wave number for the observed wave pattern near the free surface is prescribed by the rough-bed's periodicity, i.e. $k_w = 2\pi/L$, where L is the streamwise period of the roughness pattern. In the dispersion relationship for gravity waves, $\omega^2 = gk_w \tanh(hk_w)$, the $k_w h$ term is equal to 5.58 if the whole water depth is considered for h, or 2.29 if only the effective depth over the cubes ($h - k$) is used as a definition for the water depth h. For this range of values for $k_w h$, $\tanh(k_w h)$ almost equals unity, and waves follow the deep-water dispersion relationship, reading:

$$\omega = \sqrt{gk_w} \qquad (2)$$

Following the approach of Lighthill (2001), for a constant flow velocity U over a periodic bottom pattern, resonance occurs for

U satisfying:

$$U = U_r = \frac{\sqrt{gk_w}}{k_w} \qquad (3)$$

For the rough-bed pattern in the experiments, the resonant value is $U_r = 0.265\,\mathrm{m\,s^{-1}}$, close to the double-averaged velocity near the free surface which is equal to $0.28\,\mathrm{m\,s^{-1}}$. Also, the vertically averaged value of $\langle \bar{u} \rangle$, equal to $0.23\,\mathrm{m\,s^{-1}}$, is just below. This strongly suggest that the periodic pattern is due to wave-resonance.

It should be noted that the wave resonance is not an artefact of the submergence ratio since for a given water depth, the velocity, and therefore the Froude number, is determined by the bed's slope for uniform flow. In other words, for a given bed and desired water depth, the appearance of resonant waves depends on the Froude number given by the slope. This leads us to attempt to remove the mean motion due the waves in the present regime as follows. For deep-water gravity waves, potential theory leads to following velocity components (Lighthill, 2001):

$$
\begin{aligned}
u_{gw} &= A e^{k_w(z-z_{fs})} \cos(k_w(x-x_0)) \\
w_{gw} &= A e^{k_w(z-z_{fs})} \sin(k_w(x-x_0))
\end{aligned}
\qquad (4)
$$

where A is the wave amplitude (in m), z_{fs} the location of the free surface and x_0 the position of the velocity maximum. The time-averaged flow velocity fields $\bar{u}$ and $\bar{w}$ in the upper region of the flow ($1.75 < z/k < 1.95$) were used to fit the theoretical wave-pattern given by Eq. (4) in each measurement plane, the amplitude A and x_0 being the free parameters. The values obtained are given in Table 2 and it can be seen that A varies little between the three planes for both the longitudinal and the vertical velocity component. Nevertheless, the amplitude tends

Table 2 Fitted values of the wave amplitude A and x_0 for the streamwise and vertical velocity components u_{gw} and w_{gw}

	Plane (A)		Plane (B)		Plane (C)	
	u_{gw}	w_{gw}	u_{gw}	w_{gw}	u_{gw}	w_{gw}
A (cm s^{-1})	0.85	0.72	0.99	0.92	1.16	1.11
x_0 (cm)	1.21	1.11	1.51	1.39	1.68	1.75

to decrease slightly from plane (A) to plane (C), indicating a weak 3D wave structure.

Finally, to allow analysis of the mean flow variation without wave contribution, the contribution of the gravity wave described by Eq. (4), using the values of A and x_0 found by fitting in the upper part of the flow, was subtracted from the mean flow. The resulting longitudinal and vertical mean flow velocity components are plotted in Fig. 7. When compared to Figs 4d–f and 6d–f, the velocity fields with the removed wave contribution clearly exhibit the same properties near the rough bed since the exponential decay of the wave components is essentially negligible in the lower part of the flow.

Back to Fig. 4g–i, it can be seen that for the lower relative submergence $h/k = 1.5$, the longitudinal mean velocities have a monotonically decreasing behaviour in each of the planes as for $h/k = 3$. It can also be seen that the streamwise velocity component is overall far higher in plane (A) than in the two other planes (B) and (C), a signature of the development of preferential alleys for the flow in the longitudinal direction (Fig. 4g–i). In plane (C), located directly above the cubes, the longitudinal velocity component increases drastically as the flow passes above the cubes, and diminishes in the inter-space between two consecutive cubes. Indeed, the gravity-wave resonance is not observed any more and the free surface acts now as a rigid roof which constrains the flow in the vertical direction.
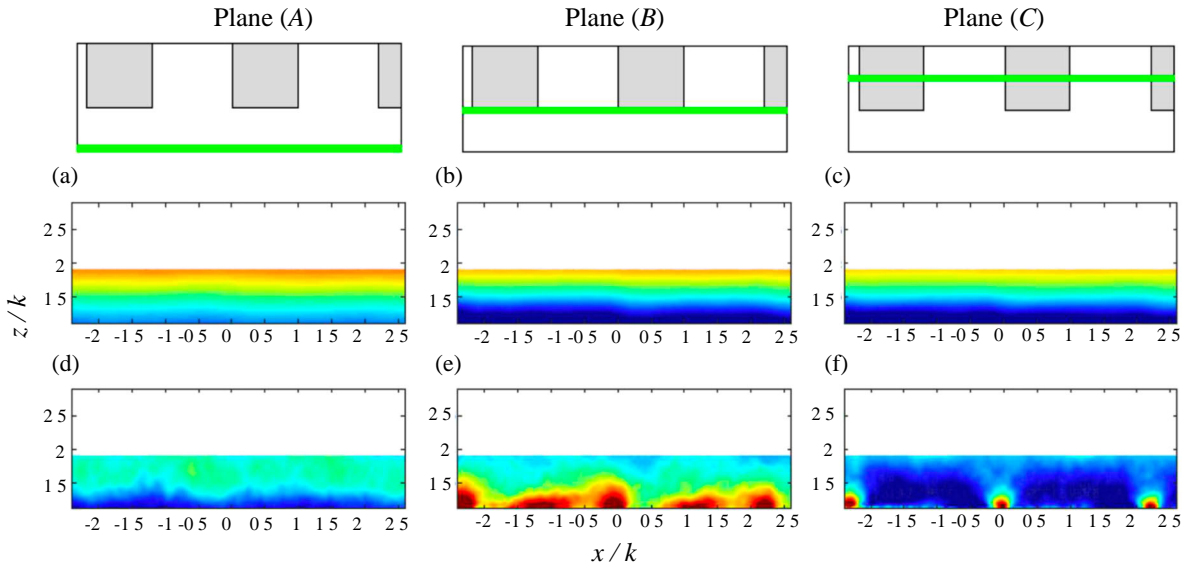

Figure 7 Time-averaged velocity fields for $h/k = 2$ after subtraction of the surface gravity-wave contribution in measurement planes (A), (B) and (C). (a), (b) and (c): $\bar{u}/u_*$; (d), (e) and (f): $\bar{w}/u_*$. Scale map colours are the same as in Figs 4 and 6 for $\bar{u}/u_*$ and $\bar{w}/u_*$, respectively

It is also apparent that $\bar{w}$ increases significantly at the upstream edge of the cube, as seen in Fig. 6g–i. The vertical velocity exhibits very specific behaviour: it exhibits positive values for plane (B), and negative values the two other planes, (A) and (C). For the latter two planes, the values are decreasing over depth and are symmetrical with respect to plane (B). This behaviour is significant and indicates that secondary flows occur in the (y,z)-plane at the roughness-pattern length-scale for $h/k = 1.5$. The lateral velocity $\bar{w}$ confirms these observations. In particular, in Fig. 5g–i, $\bar{w}$ decreases from high positive values near the cubes to strong negative values near the free surface in the intermediate plane (B).

3.2 Single-plane and five-plane double-averaged velocities

To compare the time-averaged velocity fields between the different planes, the three velocity components were time and spatially averaged in the longitudinal direction over one wavelength in each plane, yielding quantities noted $\langle \bar{u}_i \rangle_x$. The five-plane double-averaged velocity components $\langle \bar{u}_i \rangle$ are then easily computed by using the three spatially-averaged planes with the two additional planes (B') and (B'') obtained by symmetry considerations from plane (B) (Fig. 2), yielding spatially converged double-averages over the roughness pattern (Section 2.2). The gravity waves in flow regime $h/k = 2$ were removed as described in the previous section.

Figure 8a–i shows the single-plane double-averaged $\langle \bar{u}_i \rangle_x / u_*$ and the five-plane double-averaged $\langle \bar{u}_i \rangle / u_*$ velocity components for the three submergence ratios. It can be seen in Fig. 8a that the three profiles of the streamwise velocity component $\langle \bar{u} \rangle_x / u_*$ collapse well in the outer layer for the higher relative submergence ratio $h/k = 3$. Of course, this quantity does not follow the same tendency in the different planes when approaching the roughness elements. There, the vertical profiles deviate from each other, marking an increase of the spatial variation indicative of the presence of the roughness sublayer. The same behaviour is found for the lower submergence flow regimes (Fig. 8d and 8g). However, as h/k decreases, the inter-plane variation strengthens, associated with the overall velocity increase in the inter-cube preferential alley of plane (A). For $h/k = 1.5$, the inter-plane variation extends up to the free surface.

For the highest relative submergence, $h/k = 3$, the five-plane double-averaged lateral and vertical velocity profiles (Fig. 8b and 8c) are close to zero throughout the whole water column, as expected for a 2D uniform flow. The single-plane averages, however, reveal non-zero values, in particular as the roughness crests are approached.

For the intermediate relative submergence, $h/k = 2$, the single-plane averaged profiles for all three velocity components (Fig. 8d–f) remain very similar to those for $h/k = 3$ up to their maximum overlapping height of $z/k = 2$. Yet, the longitudinal velocity profiles $\langle \bar{u} \rangle_x / u_*$ and $\langle \bar{u} \rangle / u_*$ are overall higher for $h/k = 2$ than for $h/k = 3$, and the lateral and vertical velocity

profiles $\langle \bar{v} \rangle_x / u_*$ and $\langle \bar{w} \rangle_x / u_*$ show an increase of the inter-plane variation.

For the lowest relative submergence ratio, $h/k = 1.5$, the single-plane averaged profiles of the lateral and vertical velocity components follow the same general trend as for higher values of h/k for overlapping heights ($z/k < 1.5$) but differences appear. $\langle \bar{v} \rangle_x / u_*$ and $\langle \bar{w} \rangle_x / u_*$ are now mostly non-zero in all planes throughout the water depth, indicating secondary currents at the roughness scale. However, at larger scale, only fully double-averaged profiles are relevant for such an interpretation, given here by the five-plane double-averaged profiles $\langle \bar{v} \rangle / u_*$ and $\langle \bar{w} \rangle / u_*$. These are very close to zero, confirming the 2D behaviour of the flow larger than the roughness scale. For the streamwise mean flow, it can be seen that the vertical profile of $\langle \bar{u} \rangle_x / u_*$ in plane (A) clearly departs more from the same profiles in planes (B) and (C) than for the higher h/k ratios, illustrating the growing preference of the flow for the alley between the cubes as the submergence ratio decreases. Quantitatively, at $z/k = 1.2$, the ratio of $\langle \bar{u} \rangle_x / u_*$ in plane (A) to the five-plane double-averaged velocity $\langle \bar{u} \rangle / u_*$ is only equal to 1.10 at $h/k = 3$ but increases to 1.32 at $h/k = 1.5$.

In Fig. 9a–c, the five-plane double-averaged velocities for the three submergence ratios are superposed for each of three velocity components. Figure 9a shows a gradual increase of the whole vertical profile of the double-averaged longitudinal velocity $\langle \bar{u} \rangle$ with decreasing h/k, indicating that, as h/k decreases, the rough bed becomes hydraulically rougher, a trend that will be confirmed by the friction velocity in Section 5.

In Fig. 9b and 9c, it can be seen that both the lateral and the vertical double-averaged velocity are very close to zero (less than about 0.5% of $\langle \bar{u} \rangle / u_*$), as would be expected for a developed, uniform and homogeneous flow. Nevertheless, for the profile of $\langle \bar{w} \rangle$ of flow regime $h/k = 3$ in Fig. 9c, the linear decrease from a negative value at the top to a zero value at $z/k \approx 1.2$ can be attributed to a slight non-uniformity of the flow, in accordance with the 1% non-uniformity level given previously. However, the profiles of $\langle \bar{w} \rangle$ for $h/k = \{1.5, 2\}$ and the systematic trend towards positive values of $\langle \bar{w} \rangle$ near the bed for all three regimes, increasing with decreasing values of h/k, suggests a small bias error due to a lack of spatial convergence of the five-plane double-averaged vertical velocity in the highly non-uniform region near the bed. As for the vertical profiles of the double-averaged transverse velocity $\langle \bar{v} \rangle$ in Fig. 9b, the small non-zero values, considering the symmetry of the flow (near zero values in planes (A) and (C), and opposite values in planes (B) and (B')), are more likely due to a slight misalignment of the laser-sheet with the flow (around the vertical axis), leading to a projection error. An angle error as low as 0.3°, approximately the measurement accuracy, explains the non-zero values across the water depth for $h/k = 3$ and 2. The non-zero values of regime $h/k = 1.5$ near the bed are likely again due to a lack of spatial convergence.

In summary, the highest, yet still low, relative submergence ratio of $h/k = 3$ exhibits the classical roughness sublayer
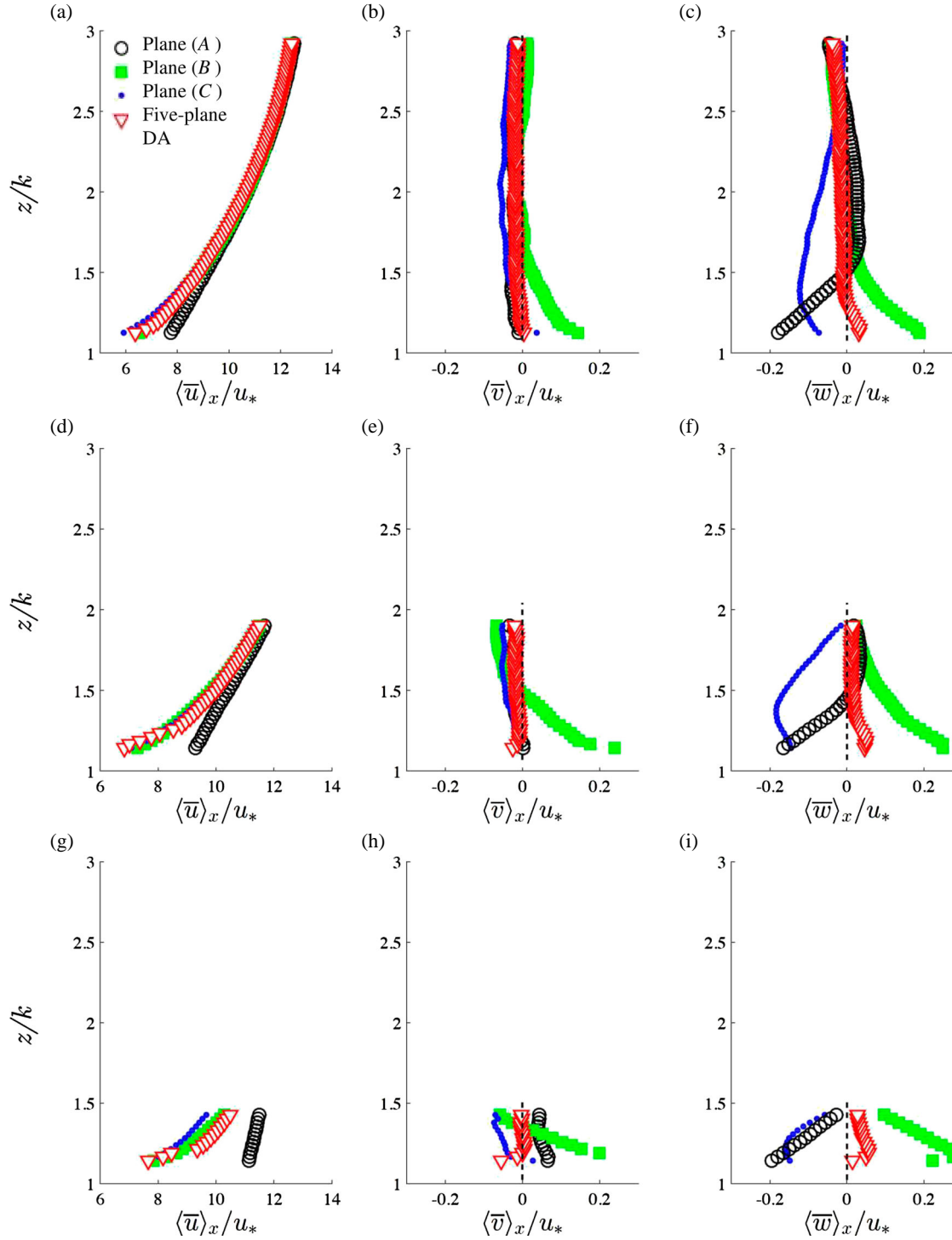
Figure 8 Normalized vertical profiles of the time- and single-plane averaged streamwise, lateral and vertical velocity components for measurement planes (A), (B) and (C). (a), (b) and (c): $h/k = 3$ (E06); (d), (e) and (f): $h/k = 2$ (E04); (g) (h) and (i): $h/k = 1.5$ (E03). The five-plane double-averaged profiles $\langle \bar{u} \rangle / u_*$, $\langle \bar{v} \rangle / u_*$, $\langle \bar{w} \rangle / u_*$ are plotted by red triangles

characteristics with mean spatial variations in the sublayer and collapsing single-plane averaged profiles above, for all three velocity components. At the intermediate low relative submergence, $h/k = 2$, the five-plane double-averaged profiles exhibit a similar behaviour as for $h/k = 3$ and the inter-plane variation also remains similar. Since the vertical extent of inter-plane variation is roughly scaling with k, the roughness sublayer

approaches the free surface closer for $h/k = 2$. Surface water-waves were also generated for this regime, but whether the waves are removed as in Fig. 8g–i, or not, the five-plane double-averaged profiles are unaffected (not shown) since the wave pattern has the same periodicity as the rough bed. Finally, the mean flow distribution is clearly different only for the lowest relative submergence, $h/k = 1.5$, the square roughness-element
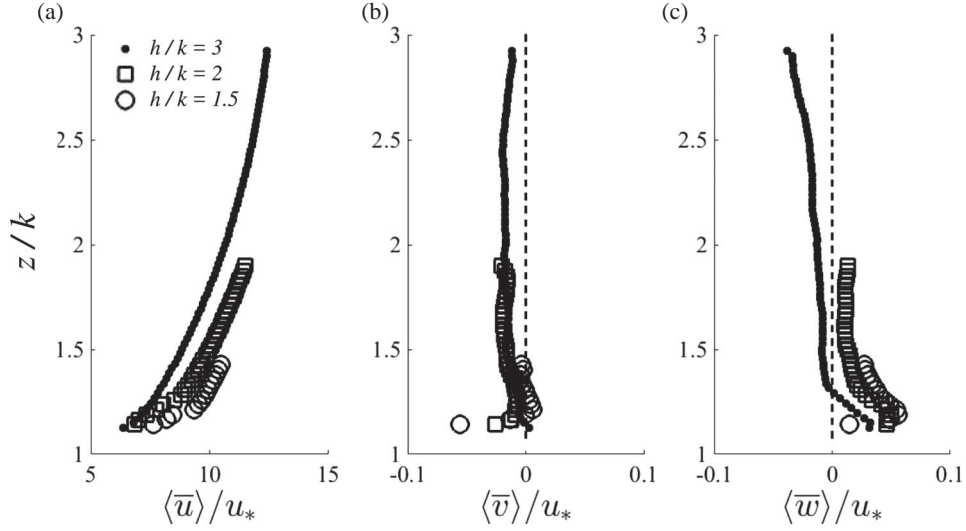
Figure 9   Normalized five-plane double-averaged velocities for $h/k = 3$, $h/k = 2$ and $h/k = 1.5$. (a) $\langle \overline{u} \rangle / u_*$, (b) $\langle \overline{v} \rangle / u_*$, and (c) $\langle \overline{w} \rangle / u_*$
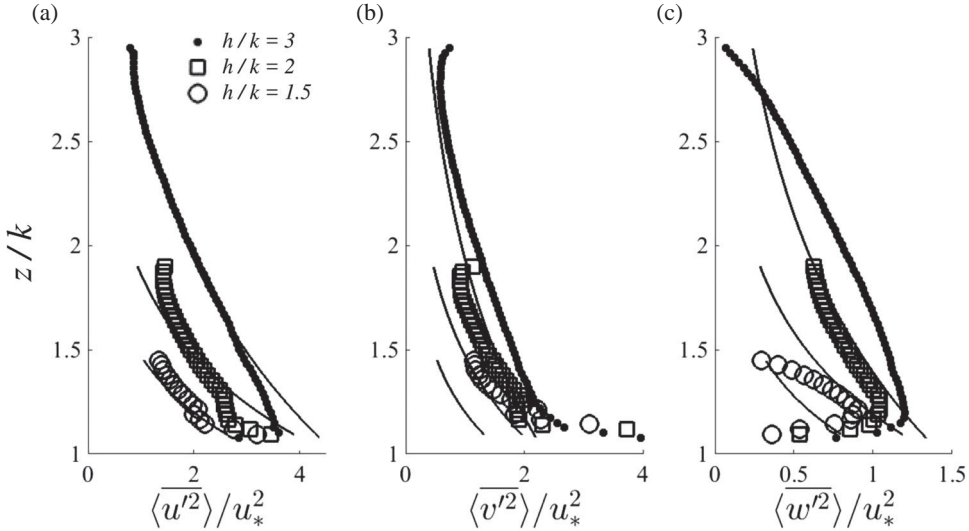

Figure 10   Normalized spatially-averaged normal stresses for $h/k = 3$, $h/k = 2$ and $h/k = 1.5$. (a) $\langle \overline{u'^2} \rangle / u_*$, (b) $\langle \overline{v'^2} \rangle / u_*$ and (c) $\langle \overline{w'^2} \rangle / u_*$. The exponential laws of Nezu and Nakagawa (1993) are plotted as thin lines

configuration leading to an increased streamwise and lateral flow in the inter-cube alley, the (A)-plane, as well as secondary flow at the roughness-scale throughout the water depth. The difference in streamwise velocity across the planes, in particular with plane (A), is of the same order as the vertical velocity gradient, suggesting a comparable generation of turbulent normal and shear-stresses in the lateral direction.

3.3   Five-plane spatially-averaged stresses

The vertical profiles of the five-plane spatially-averaged normal stresses normalized by u_*^2 are plotted for the three relative submergence ratios in Fig. 10a–c for the three velocity components, respectively. Also plotted in each figure and for each submergence ratio are the exponential fitting laws proposed by Nezu and Nakagawa (1993) for high-submergence open-channel measurements. It can be seen in Fig. 10a that relatively

good accordance with those laws for all three submergence ratios is found for the streamwise velocity component $\langle \overline{u'^2} \rangle / u_*^2$. For the vertical component $\langle \overline{w'^2} \rangle / u_*^2$, shown in Fig. 10c, the data globally overlap but the curvatures are different. Yet, referring to the original data of Nezu and Nakagawa (1993) plotted in their fig. 4.7, one can observe that an exponential is not necessarily the best fit to the scattered data and could well follow the clear trend of the present data. It should also be noted that the trends of $\langle \overline{w'^2} \rangle / u_*^2$ are very similar between $h/k = 3$ and 1.5, unlike for $h/k = 2$ at which $\langle \overline{w'^2} \rangle / u_*^2$ increases towards the free surface. In the latter regime, however, the remaining unstationary and weak lateral waves coupled to the streamwise resonant wave are likely to cause the higher vertical normal stress. For the lateral normal stress $\langle \overline{v'^2} \rangle / u_*^2$ shown in Fig. 10b, the trends are similar, lying marginally above the exponential fit of Nezu and Nakagawa (1993), except for $h/k = 1.5$, where the data lie significantly higher although still following the same trend.

These increased normal stresses can be related to increased turbulence production associated with the strong lateral inter-plane shear observed in the previous section for this very low submergence regime (Fig. 8g). For the two higher submergence ratios investigated, this effect as seen in the inter-plane comparisons in Fig. 8a and 8d, is much weaker.

In the framework of the double-averaging methodology, all time-averaged quantities $\bar{\phi}$ are decomposed into a time- and spatially-averaged component $\langle\bar{\phi}\rangle$ and a dispersive component $\tilde{\phi}$, defined as:

$$\bar{\phi}(x,y,z) = \langle\bar{\phi}\rangle(z) + \tilde{\phi}(x,y,z)$$

In the double-averaged momentum equations, the total shear stress tensor τ_{ij} at level z reads:

$$\frac{\tau_{ij}}{\rho} = -\langle\overline{u'_i u'_j}\rangle - \langle\tilde{u}_i\tilde{u}_j\rangle + \nu\frac{\partial\langle\overline{u_i}\rangle}{\partial x_j} \qquad (5)$$

where $-\langle\overline{u'_i u'_j}\rangle$ is the spatially-averaged Reynolds stress, $-\langle\tilde{u}_i\tilde{u}_j\rangle$ is the dispersive stress (or form-induced stress) and $\nu\partial\langle\overline{u_i}\rangle/\partial x_j$ is spatially-averaged viscous stress.

The spatially-averaged Reynolds stress, dispersive stress and total shear stress as well as the viscous stress resulting from the vertical shear are plotted in Fig. 11a–i for the three submergence ratios. The viscous stresses are multiplied by a factor of 10. It can be seen in Fig. 11a that the viscous stresses are more than one order of magnitude smaller than all other terms of the total shear stress tensor. The profiles of the normalized total stress in the longitudinal plane, $\tau_{xz}/(\rho u_*^2)$, shown in Fig. 11g, are linear, confirming that the flow is uniform and two-dimensional without secondary circulations. The non-normalized profiles are used to determine the friction velocities u_* for the three regimes (given in Table 1) by extrapolating the linear behaviour towards $z=k$. It should be noted that this friction velocity u_* as defined here is not the friction velocity for the bed stress τ_0 but rather the turbulent velocity scale at the top of roughness. It is the appropriate velocity to scale the turbulence though (Florens, 2010; Pokrajac, Finnigan, Manes, McEwan, & Nikora, 2006). As shown by Pokrajac et al. (2006), τ_0 is larger than τ_k (defined as $\tau_k = \rho u_*^2$), given by $\tau_0/\tau_k = (1 + \Phi k/h)$ where Φ is the canopy porosity ($\Phi = 0.80$ in the present experiments). In rough boundary layers with high relative submergence, the difference between the two scales becomes negligible but not for the low submergence regimes considered here.

Concerning the dispersive stresses in the longitudinal plane $\langle\tilde{u}\tilde{w}\rangle/u_*^2$, it can be seen in Fig. 11d that as h/k decreases, the relative contribution of the dispersive term to the associated total shear stress $\tau_{xz}/(\rho u_*^2)$ increases. In all cases though, it is not negligible as has often be concluded in studies with low spatial resolution measurements (e.g. Coceal et al., 2006; Jiménez, 2004; Macdonald, 2000). Indeed, as shown by Florens et al. (2013) whose measurements encompassed the interstitial

flow in the canopy, the dispersive shear stress reaches a maximum just below the roughness crest at $z/k \approx 0.8$, peaking at $\langle\tilde{u}\tilde{w}\rangle/u_*^2 \approx 1.4$ for the same rough bed as in this study but for higher submergence ($h/k = 6.7$). It may be noted that the obvious difficulty of measuring the maximum dispersive stresses and defining the roughness sublayer height (discussed later in Section 4.2) by a threshold percentage of the maximum measured dispersive stresses, has led to largely overestimated heights.

Finally, the two other total-stress tensor components, τ_{xy} and τ_{yz}, are an order of magnitude below the τ_{xz} component, and are almost equal to zero everywhere as expected for a uniform flow. The same remark applies to $-\langle\overline{u'v'}\rangle$, $-\langle\overline{v'w'}\rangle$, $-\langle\tilde{u}\tilde{v}\rangle$ and $-\langle\tilde{v}\tilde{w}\rangle$ that are also very close to zero, as expected. The small yet unexpected deviations towards the top of the roughness crests in the $u-v$ component stresses (Fig. 11b, e, h) could be due to the small error in laser-sheet alignment previously invoked to explain non-zero values of the five-plane double-averaged transverse velocity. A small rotation around the vertical axis is sufficient to contaminate $-\langle\tilde{u}\tilde{v}\rangle$, theoretically zero everywhere, with a small amount of $\langle\tilde{u}\tilde{u}\rangle$ which increases in the roughness sublayer.

3.4 Five-plane spatially-averaged skewness

Vertical profiles of the five-plane spatially-averaged skewness for the three velocity components are plotted in Fig. 12a–c, respectively, for the three flow regimes. For the lateral skewness $S_v = \langle\overline{v'^3}\rangle/\langle\overline{v'^2}\rangle^{3/2}$, values close to zero are recovered for all the profiles (except near the roughness crests for same as reasons as just discussed but with even higher sensitivity to convergence due to the higher-order statistics), confirming again the lateral invariance, i.e. the two-dimensionality of the flow.

For the streamwise skewness, $S_u = \langle\overline{u'^3}\rangle/\langle\overline{u'^2}\rangle^{3/2}$, negative values are found, as already observed in the external part of canonical turbulent boundary layers over smooth or highly submerged rough beds above $z/\delta > 0.05$ (e.g. Squire et al., 2016). In open-channel flows, the decrease of the streamwise skewness towards values as low as -3 near the top of the turbulent boundary-layer height as documented by Squire et al. (2016) is limited by the presence of the free surface. In Al Faruque and Balachandar (2011), for open-channel experiments over a highly submerged rough bed, S_u reaches a minimum at mid-depth with a value there of -0.4 as inferred from the data available in the article. It corresponds also to the value found by Squire et al. (2016) at $(z + \epsilon)/\delta_{99} = 0.5$, well below where the maximum is found in canonical boundary layers. This suggests that the free surface reduces the skewness in the top part of the outer layer. In the present experiments, the flow with $h/k = 3$ and $h/k = 2$ clearly exhibits the same behaviour, a slight decrease of S_u towards a maximum value close to -0.5 near $z/k = 2.3$ and $z/k = 1.7$, respectively, before a sharper increase back towards zero near the free surface. The trend for $h/k = 1.5$ is similar with a weakly defined peak at a lower value
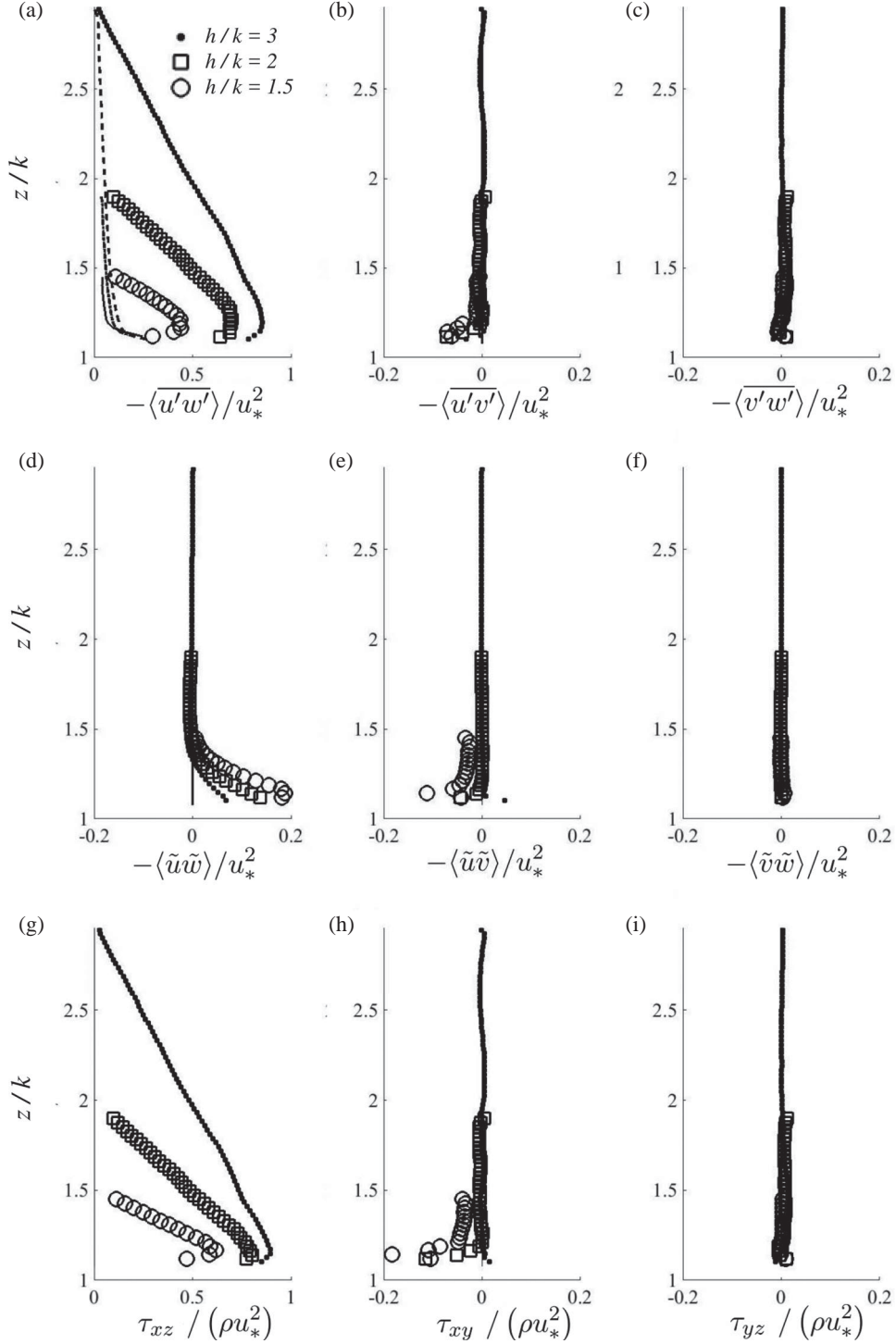
Figure 11 Normalized five-plane spatially-averaged stresses for $h/k = 3$ (•), $h/k = 2$ (□) and $h/k = 1.5$ (○). (a), (b) and (c): spatially-averaged Reynolds stresses $-\langle \overline{u'w'} \rangle$, $-\langle \overline{u'v'} \rangle$ and $-\langle \overline{v'w'} \rangle$; (d), (e) and (f): dispersive stresses $-\langle \tilde{u}\tilde{w} \rangle$, $-\langle \tilde{u}\tilde{v} \rangle$ and $-\langle \tilde{v}\tilde{w} \rangle$; (g) (h) and (i): total stresses τ_{xz}, τ_{xy} and τ_{yz}. In (a), the spatially averaged viscous stresses $\nu \partial \langle \bar{u} \rangle / \partial z$ are also given and are multiplied by 10: (——) $h/k = 3$, (. . .) $h/k = 2$ and (——) $h/k = 1.5$

of about -0.4 near $z/k = 1.2$. These peaks are close to an effective relative water depth of about 0.7, except for $h/k = 2$ which is roughly around 0.8. Interestingly, the 0.7 value is close to the lower bound of the classical free-surface influenced layer at around 0.6 (e.g. Nezu & Nakagawa, 1993). The $h/k = 2$ regime again is likely to be influenced by the surface waves.

For the vertical skewness $S_w = \langle \overline{w'^3} \rangle / \langle \overline{w'^2} \rangle^{3/2}$, positive values are found, with a similar behaviour for $h/k = 3$ and $h/k = 2$. In open-channel turbulent boundary layer flows over highly submerged rough beds, Al Faruque and Balachandar (2011) and Hanmaiahgari, Roussinova, and Balachandar (2017) show highly antisymmetric vertical profiles of the streamwise and
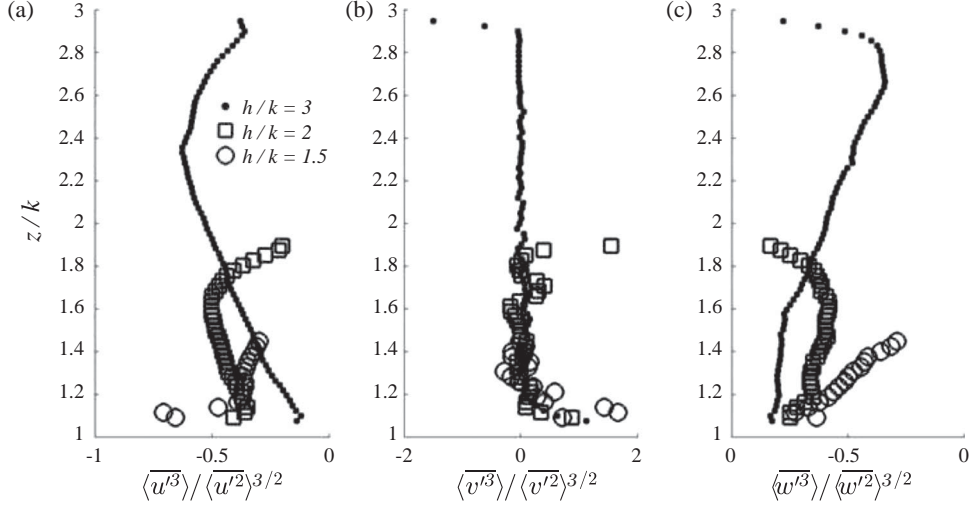
Figure 12   Five-plane spatially-averaged skewness for $h/k = 3$ (•), $h/k = 2$ (□) and $h/k = 1.5$ (○). (a) $S_u = \langle \overline{u'^3} \rangle / \langle \overline{u'^2} \rangle^{3/2}$; (b) $S_v = \langle \overline{v'^3} \rangle / \langle \overline{v'^2} \rangle^{3/2}$; (c) $S_w = \langle \overline{w'^3} \rangle / \langle \overline{w'^2} \rangle^{3/2}$

vertical skewnesses S_u and S_w as seen here, albeit with an upwards shift of the peak of $S_w = \langle \overline{w'^3} \rangle / \langle \overline{w'^2} \rangle^{3/2}$ for $h/k = 3$. With the same adimensionalization as in the present work (i.e. using $\langle \overline{w'^2} \rangle^{3/2}$), values close to 0.5 are found at mid-depth in their data, in accordance with our own measurements. At $h/k = 1.5$, however, the vertical skewness S_w clear shows a different trend, growing linearly along the whole depth instead of exhibiting a local maximum as for $h/k = 2$ and $h/k = 3$.

4   Roughness sublayer analysis

4.1   *Spatial standard deviation*

The spatial standard deviation (or dispersion) of a time-averaged quantity $\bar{\phi}(x, y, z)$ is defined as:

$$D_s \left(\bar{\phi} \right) = \sqrt{\langle \tilde{\phi}^2 \rangle} \qquad (6)$$

The estimation of the dispersive component $\tilde{\phi}$ is biased by the finite number of samples in the time series, i.e. the calculated spatial standard deviation includes both the true spatial standard deviation and an artificial standard deviation due to the time convergence error (Florens et al., 2013). As shown in Florens et al. (2013), the two contributions are not correlated, and therefore the time convergence error contribution can be removed in order to better estimate the true spatial standard deviation. The same approach was applied here to all measurements for a better estimate of the true spatial standard deviation.

Figure 13a–c presents the resulting spatial standard deviation $2D_s$ of the time-averaged velocities $\bar{u}$, $\bar{v}$ and $\bar{w}$, all normalized by the double-averaged streamwise velocity component $\langle \bar{u} \rangle$. The factor 2 is chosen to relate the spatial standard deviation to the time-conversion error which is statistically estimated with 95% confidence (Florens et al., 2013). For $h/k = 3$, the spatial standard deviation approaches zero when approaching the

free surface, except for the vertical component which deviates almost imperceptibly (Fig. 13c), probably because of the slight non-uniformity of the flow. For the intermediate regime $h/k = 2$, the spatial standard deviations with and without the wave contribution are plotted. When the wave pattern is subtracted, the main effect is to suppress the increase of spatial standard deviation associated with the wave near the free surface. As h/k decreases further to 1.5, the normalized spatial standard deviation increases rapidly. This increase of the spatial standard deviation is generated by the combination of the free-surface constraint and the flow preference for the alley between the cubes, as discussed in the previous section. It is also worth noting that the spatial standard deviation of the streamwise velocity component as the canopy is approached is an order of magnitude higher than the other two velocity components.

The spatial standard deviations $2D_s$ of the normal stresses $\overline{u'^2}$, $\overline{v'^2}$ and $\overline{w'^2}$ are plotted in Fig. 13d–f, respectively, and of the turbulent shear stresses $-\overline{u'w'}$, $-\overline{u'v'}$ and $-\overline{v'w'}$ in Fig. 13g–i, respectively, all with the same normalization as in Florens et al. (2013). Similar behaviour as found for the spatial standard deviation of the time-averaged velocities is observed here. As expected for $h/k = 3$, the spatial standard deviation of the normal stresses tends to zero in the outer layer for $z/k > 1.5$, but only for $\overline{u'^2}$ and $\overline{v'^2}$. The spatial standard deviation of $\overline{w'^2}$ increases again as the free surface is approached, an artefact which is due to the scaling chosen in Florens et al. (2013) since the spatially-averaged turbulent stress $\langle \overline{w'^2} \rangle$ goes to zero at the free surface. For the same reason, it can be seen in Fig. 13g–i that the spatial standard deviation of the three shear stresses monotonically increase as the free surface is approached. The spatial standard deviation profiles for the intermediate case $h/k = 2$ with or without the wave contribution are almost identical for all second-order statistics.

When comparing with the spatial standard deviation profiles of Florens et al. (2013) at $h/k = 6.7$, the profiles for $h/k = 3$ presented here are in very good agreement in the overlap range
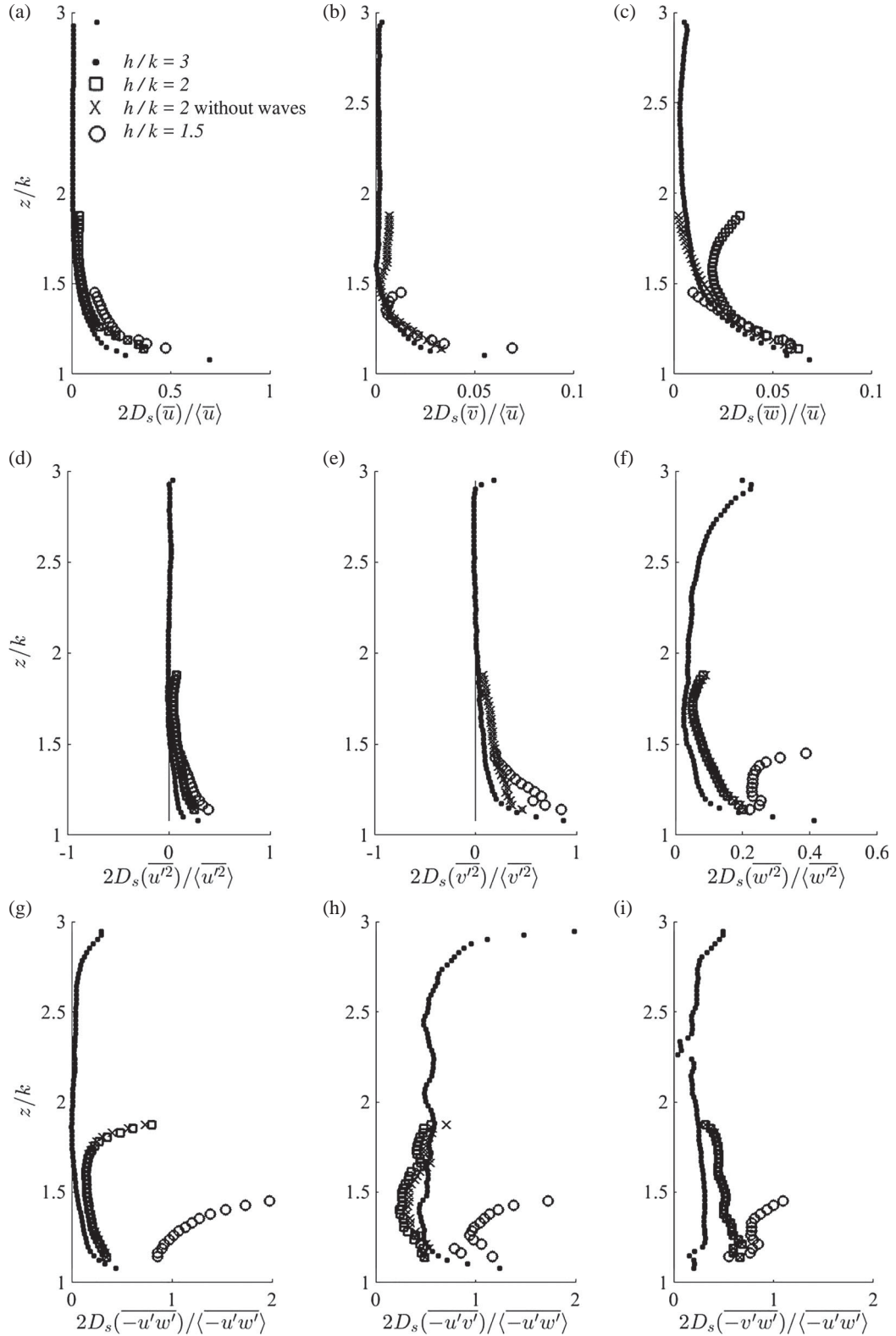
Figure 13   Normalized spatial standard deviations $2D_s(\bar{\phi}) = 2\sqrt{\langle \tilde{\phi}^2 \rangle}$ for $h/k = 3$ (•), $h/k = 2$ with resonant wave (□) and with resonant wave removed (X) and $h/k = 1.5$ (○). (a), (b) and (c): $\bar{\phi} = \bar{u}$, $\bar{v}$ and $\bar{w}$; (d), (e) and (f): $\bar{\phi} = \overline{u'^2}$, $\overline{v'^2}$ and $\overline{w'^2}$; (g) (h) and (i): $\bar{\phi} = -\overline{u'w'}$, $-\overline{u'v'}$ and $-\overline{v'w'}$. All spatial standard deviations are normalized by the corresponding double-averaged quantity when possible, or by the closest equivalent if it is expected to be equal to zero along the whole profile

$1.2 < z/k < 3$ (Rouzes, 2015). This suggests that the roughness sublayer for both flow regimes is very similar. However, for the two lower h/k regimes, the spatial standard deviation profiles do not follow the same trend any more, indicating a modification of the roughness sublayer structure. This evolution with h/k is discussed more quantitatively in the next subsection.

	$h/k = 6.7$ Florens et al. (2013)	$h/k = 3$ Eiff et al. (2014)	$h/k = 3$	$h/k = 2$ with waves	$h/k = 2$ without waves	$h/k = 1.5$
$\bar{u}$	1.2	1.4	1.4	1.5	1.5	1.5
$\bar{v}$	–	–	1.1	1.1	1.1	1.15
$\bar{w}$	1.10	1.1	1.1	1.2	1.2	1.2
$\overline{u'^2}$	1.1	1.2	1.3	1.6	1.6	1.5
$\overline{v'^2}$	–	–	1.7	1.9	1.9	1.5
$\overline{w'^2}$	1.25	1.2	1.4	1.6	1.6	1.5
$-\overline{u'w'}$	1.25	1.6	1.5	2	2	1.5
$-\overline{u'v'}$	–	–	$2D_s(\bar{\phi})/\langle\bar{\phi}\rangle > 5\%$ everywhere			
$-\overline{v'w'}$	–	–	1.6	2	2	1.5

[a] Statistics calculated with a 5% threshold upon the normalized spatial standard deviation of the time-averaged flow, $2D_s$. For the intermediate relative submergence, $h/k = 2$, results both with and without surface gravity wave are given. The results for $h/k = 6.7$ are taken from Florens et al. (2013) and those for $h/k = 3$ are computed from the experimental data described in Eiff et al. (2014)

4.2 *Roughness sublayer height*

Following the definition of the roughness sublayer as the layer of mean-flow spatial heterogeneity induced by the roughness elements (Florens et al., 2013; Pokrajac et al., 2007), the spatial standard deviation profiles plotted in the last subsection suggest that the roughness sublayer height begins to increase for $h/k < 3$. The decreasing free-surface level as h/k decreases appears to extend the roughness sublayer across the whole water column.

To quantify this trend, the top of the roughness sublayer, noted h_{rs}, is defined as the height where the non-dimensional spatial standard deviation $2D_s(\bar{\phi})/\langle\bar{\phi}\rangle$ of each profile in Fig. 13 is equal to 5%, as in Florens et al. (2013). The resulting heights, normalized by k, are given in Table 3 for the three flow regimes investigated and for the regimes of Florens et al. (2013) and Eiff et al. (2014). For $h/k = 3$, both the regime investigated here (Fr = 0.55) and the one of Eiff et al. (2014) (Fr = 0.21) give $h_{rs}/k = 1.4$ for the mean longitudinal velocity spatial standard deviation. For the other statistics at $h/k = 3$, h_{rs}/k is in the range [1.1, 1.7]. For $h/k = 2$, h_{rs}/k slightly increases for all investigated quantities with $h_{rs}/k = 1.5$ for the mean longitudinal velocity spatial standard deviation. At $h/k = 1.5$, the roughness sublayer occupies the whole water column for most quantities, i.e. h_{rs}/k levels out at 1.5.

There is a trend suggesting that the roughness sublayer height relative to the roughness element height is not independent of the relative submergence, with a tendency to increase with decreasing h/k and saturating at $h_{rs}/k = 1.5$. However, the increase can be considered small and it is tempting then to approximate the roughness sublayer height as being almost h/k independent, around $1.5h$ for the mean longitudinal velocity for the roughness pattern presented here. With such an approximation, highly submerged flows can be defined more specifically as flows for which the water depth exceeds the height of the roughness sublayer. Here, flows with $h/k > 1.5$ can then be considered as highly submerged in the sense that a region with negligible spatial standard deviation exists towards the free surface, where the measurement along a unique vertical profile is sufficient for the outer flow description. In contrast, for flows with $h/k \lesssim 1.5$, the whole water depth exhibits strong spatial standard deviation and requires a complete description with double-averaged quantities.

5 Logarithmic law

This section examines whether the logarithmic law can still be identified under conditions of very low relative submergence ($h/k < 3$) and if so, to determine its parameters and vertical range in the water column. As discussed in Section 1, the debate centres around whether this law is still applicable in these regimes and, more generally in all boundary layers including very high submergence ($\delta/k > 40$), whether the associated von Kármán constant is a constant. As a basis for analysis we will take the double-averaged velocity profiles $\langle\bar{u}\rangle(z)$ including levels within the roughness sublayer since we do not assume *a priori* that the logarithmic law must necessarily be above the roughness-sublayer.

In order to avoid fitting three parameters u_*, d, k_s of the logarithmic law (Eq. (1)), the friction velocity u_* was directly inferred from the extrapolation of total shear stress $\tau_{xz}(z)$ at $z = k$ as discussed above (Eiff et al., 2014; Florens, 2010; Pokrajac et al., 2006). The profiles of the total shear stress shown in Fig. 11 being highly linear, the extrapolation generates an error for u_* estimated at 0.2%, 0.3% and 1% for flow regimes $h/k = 3$, 2 and 1.5, respectively.

In the first approach following the Clauser method as in Eiff et al. (2014) for higher values of h/k, the von Kármán constant κ was taken as 0.41. Linear regressions were performed in parameter space $\{z, \exp(\kappa\langle\bar{u}\rangle/u_*)\}$ using the roughness-length version of the logarithmic law, yielding the roughness length z_0 and d. With $B_r = 8.5$ for fully rough flows (Nezu & Nakagawa, 1993), k_s is then computed. The upper and lower bounds of the linear regressions, denoted respectively z_m and z_M, were freely determined by minimizing the error of the slope for all possible

ranges between $z = k$ and $z = h$. A minimum of five data points with an error of less than 5% on the slope was used to determine whether a logarithmic law exists.

However, the given bounds z_m and z_M are a relatively conservative estimate. From a practical point of view it is worthwhile to ask to what extent the uncertainty in the double-averaged velocity measurements still accommodates the optimized logarithmic law beyond those bounds. To this end, the spatial convergence error deduced from the vertical profiles of the spatial standard deviation $2D_s$ for $\bar{u}$ with 95% confidence was used, denoted by $\epsilon_{\langle\bar{u}\rangle}$. The spatial convergence error $\epsilon_{\langle\bar{u}\rangle}$ is proportional to D_s and decreases with the number of vertical profiles available (here 480). It can therefore be used to select which data points can still be considered to follow the logarithmic law below z_m and above z_M. The extended lower and upper limits are noted z_m^ϵ and z_M^ϵ, respectively.

In the second approach, κ is a free parameter. We follow the general method based on the indicator function of Spalart (1988) and Segalini et al. (2013) for smooth walls and adapted by Koll (2006) and Mohajeri et al. (2015) for rough walls. Since for rough flows the displacement height d presents an additional unknown parameter, a rough-wall indicator function:

$$\Xi = \frac{1}{u_*}\frac{\mathrm{d}\langle\bar{u}\rangle}{\mathrm{d}z}(z - d) \qquad (7)$$

cannot be used directly to determine κ. Instead, given that $u_*/(\mathrm{d}\langle\bar{u}\rangle/dz) = \kappa(z - d)$, a linear regression is first performed in parameter space $\{z, u_*/(\mathrm{d}\langle\bar{u}\rangle/dz)\}$ to estimate κ, denoted $\kappa_{h/k}$ as in Mohajeri et al. (2015). The same procedure as for the constant-κ approach is used to determine the bounds and to validate the regression. Then, as in the constant-κ approach, a second linear regression in parameter space $\{z, \exp(\kappa_{h/k}\langle\bar{u}\rangle/u_*)\}$ is performed to infer the two regression parameters d and k_s as well as the bounds z_m and z_M. The extended validity range $[z_m^\epsilon, z_M^\epsilon]$ is also calculated as for the constant-κ approach.

Finally, in order to fully describe the double-averaged velocity profile, the wake function giving the departure from the logarithmic law in the outer layer:

$$W(\eta) = \frac{2\Pi}{\kappa}\sin^2\frac{\pi}{2}\eta \qquad (8)$$

was fitted to yield Coles' wake parameter Π. Here $\eta = (z - d)/(h - d)$ is the external variable defined with the effective water depth above the displacement height. Π was obtained using the d and κ values from both methods for all regimes.

5.1 Constant-κ approach

For all three relative roughness ratios, $h/k = \{1.5, 2, 3\}$, a logarithmic law was found with the constant-κ approach. The corresponding double-averaged (five planes) velocity profiles are shown in Fig. 14a including those of Eiff et al. (2014)

for $h/k = \{3, 6.7\}$. The black-filled symbols represent the validated data points in $[z_m/k, z_M/k]$ and the grey-filled symbols the extended range $[z_m^\epsilon, z_M^\epsilon]$ based on 95% confidence. It can be seen that the validated data points clearly follow the logarithmic law for all regimes. Table 4 summarizes the resulting normalized parameters $u_*/U_{\max}$, d/k, k_s/k for each relative submergence h/k. The lower and upper bounds of the fitted logarithmic layer $[z_m/k, z_M/k]$ and the extended range $[z_m^\epsilon, z_M^\epsilon]$ are also given.

Referring to Table 4, it can be observed that $u_*/U_{\max}$ increases as h/k decreases across the measurement range from 6.7 to 1.5, indicating that the roughness exerts a higher resistance as the water depth diminishes. The equivalent sand roughness normalized by the roughness height, k_s/k, on the other hand, follows the opposite tendency, decreasing as the relative submergence ratio h/k decreases. It is about equal to the roughness height for the highest submergence ($h/k = 6$) and drops to 0.27 for the lower relative submergence ratio studied ($h/k = 1.5$). The decay suggests that k_s could scale with the water depth h, which is confirmed in Table 4 where k_s/h is seen to be approximately constant around 0.17 for all h/k. The relative displacement height d/k was found to remain essentially independent of the relative submergence h/k in the range $[3, 6.7]$ by Eiff et al. (2014), with $d/k \simeq 0.8$. Here, a slightly different value of 0.87 is found for the flow regime $h/k = 3$. This difference could be driven by a difference of Froude number values, which are larger here than in the experiments analysed in Eiff et al. (2014). For the intermediate case with $h/k = 2$, an even higher value of 0.91 is found which could be triggered by the wave resonance at the free surface, not far away from the roughness elements. Yet, despite these differences, the relative displacement height d/k appears to be relatively robust with values remaining in the range $[0.77, 0.91]$ for $h/k \in [1.5, 6.7]$, which implies that d/h is decreasing with decreasing h/k. It might be noted that the increase of the relative friction velocity $u_*/U_{\max}$ as h/k decreases appears to be counter-intuitive with regard to k_s/h being constant (and k_s/k even decreasing). However, as h/k decreases, both the wake-defect effect as measured by Coles' wake-parameter Π given in Table 4 and d/h also decrease which accounts for the increase $u_*/U_{\max}$, as seen by evaluating the logarithmic law (Eq. (1)) with the law of the wake (Eq. (8)) at $z = h$ and writing the result as follows:

$$\frac{u_*}{U_{\max}} = \left[\frac{1}{\kappa}\ln\left(\frac{h}{k_s}\right) + \frac{1}{\kappa}\ln\left(1 - \frac{d}{h}\right) + B_r + \frac{2\Pi}{\kappa}\right]^{-1} \qquad (9)$$

The lower and upper bounds z_m/k and z_M/k of the optimally fitted logarithmic law are relatively insensitive to the submergence ratios investigated. The lower bound z_m/k is close but beneath the roughness layer height h_{rs}/k given by the spatial standard deviation of $\langle\bar{u}\rangle$ criterion (Table 3). When expressed as a relative height above the displacement height, $\eta_{\max} = (z_M - d)/(h - d)$, it can be seen in Table 4 that the logarithmic layer's upper bound is close to the classical value of 0.2, with values of 0.13 and 0.29 at $h/k = 6$ and $h/k = 3$, respectively.
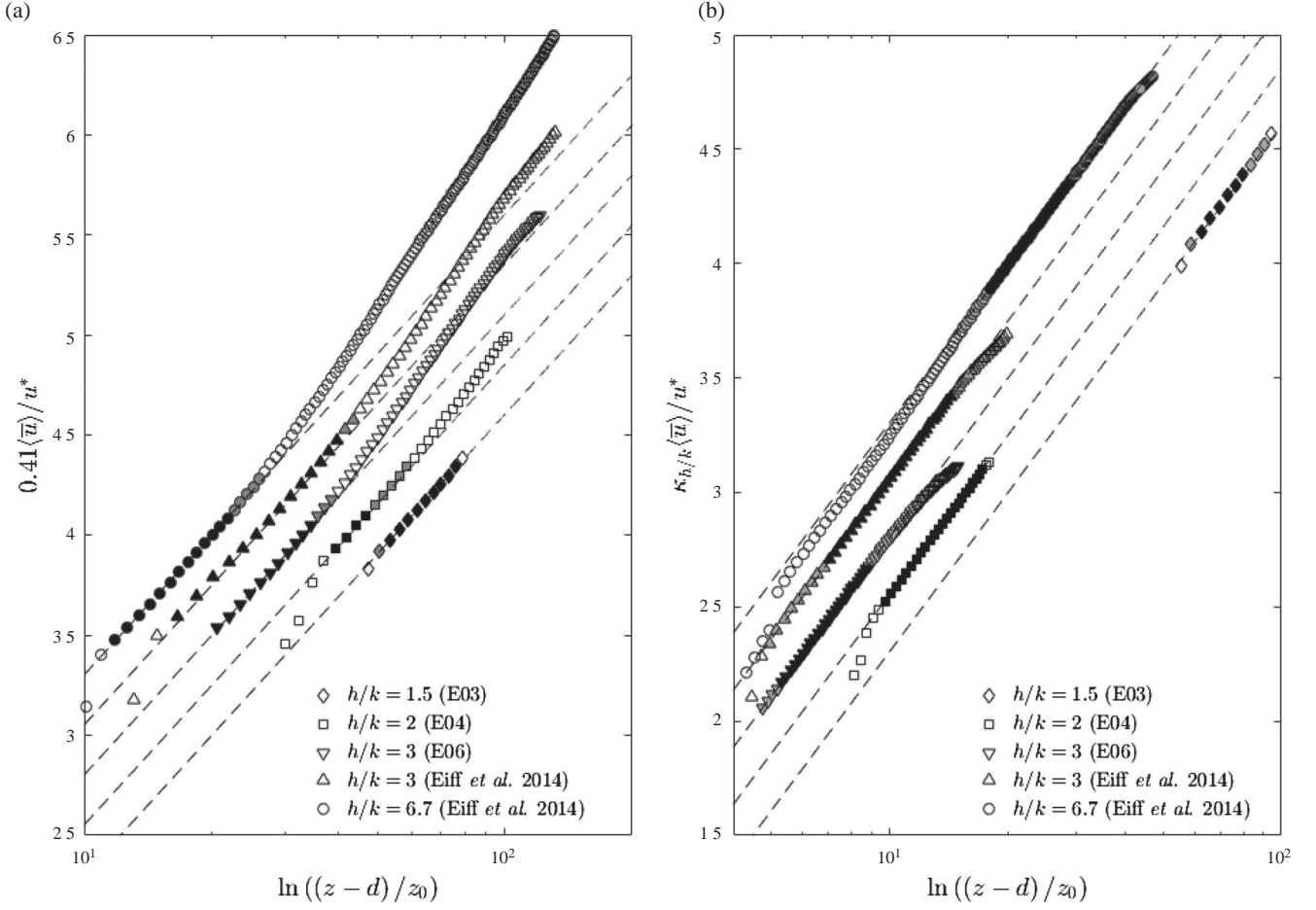
Figure 14 Vertical profiles of double-averaged velocity $\kappa\langle\bar{u}\rangle/u_*$ (symbols) along with (a) the logarithmic law obtained with the constant $\kappa = 0.41$ fitting approach and (b) the logarithmic law obtained with the free-κ fitting approach (dashed lines). For clarity, the data for the different h/k regimes are translated vertically. Filled (black) symbols correspond to the initial validated fitting range, grey symbols mark the extended validity range (see text for further explanations). Lower and upper bounds of these validity ranges are given in Tables 4 and 5

Table 4 Logarithmic-law parameters using $\kappa = 0.41$ (constant-κ approach) for all regimes investigated here and from Eiff et al. (2014)[a]

h/k	u_*/U_{max}	d/k	k_s/k	k_s/h	Π	z_m/k	z_M/k	η_{max}	z_m^ϵ/k	z_M^ϵ/k	η_{max}^ϵ
6.7 [a]	0.069	0.768 ± 0.007	1.112 ± 0.006	0.166	0.38	1.14	1.54	0.13	1.14	1.69	0.15
3 [a]	0.082	0.818 ± 0.010	0.522 ± 0.005	0.174	0.24	1.06	1.46	0.29	1.06	1.51	0.32
3 (E06)	0.079	0.869 ± 0.009	0.555 ± 0.005	0.185	0.17	1.15	1.48	0.29	1.15	1.53	0.31
2 (E04)	0.084	0.912 ± 0.003	0.324 ± 0.001	0.162	0.11	1.28	1.40	0.45	1.28	1.50	0.54
1.5 (E03)	0.085	0.825 ± 0.005	0.269 ± 0.001	0.179	0.04	1.24	1.45	0.93	1.24	1.47	0.96

The fitted logarithmic-law parameters are d, k_s, and the lower and upper bounds z_m/k and z_M/k. $\eta_{max} = (z_M - d)/(h - d)$. z_m^ϵ and z_M^ϵ are the lower and upper bounds of the logarithmic law using a spatial convergence error estimate $\epsilon_{\langle\bar{u}\rangle}$ with 95% confidence. $\eta_{max}^\epsilon = (z_M^\epsilon - d)/(h - d)$. Π is Coles' wake parameter.

For lower submergence, however, the upper bound increases, reaching $\eta_{max} = 0.93$ at $h/k = 1.5$. The extended validity range $[z_m^\epsilon, z_m^\epsilon]$ does not change these observations, with only slight differences in the upper bound. For example, the upper limit z_m^ϵ scaled by the relative depth, $\eta_{max}^\epsilon = (z_M^\epsilon - d)/(h - d)$ yields $\eta_{max}^\epsilon = 0.96$ at $h/k = 1.5$.

In summary, in the framework of a constant κ ($\kappa = 0.41$), a logarithmic law can still be observed for relative submergence ratios as low as $h/k = 1.5$ with a relative extent that increases

with decreasing h/k. For $h/k = 1.5$, this law describes almost the entire vertical extent of the double-averaged velocity profile through the water depth without a need for a defect law and is completely within the roughness sublayer. The high extent of the range beyond the usual upper bound of about 0.2 coincides with decreasing values of Coles' wake parameter Π of the wake-defect law (Table 4). This can be seen in the velocity profiles plotted in Fig. 14a where the defect almost disappears for this flow regime.
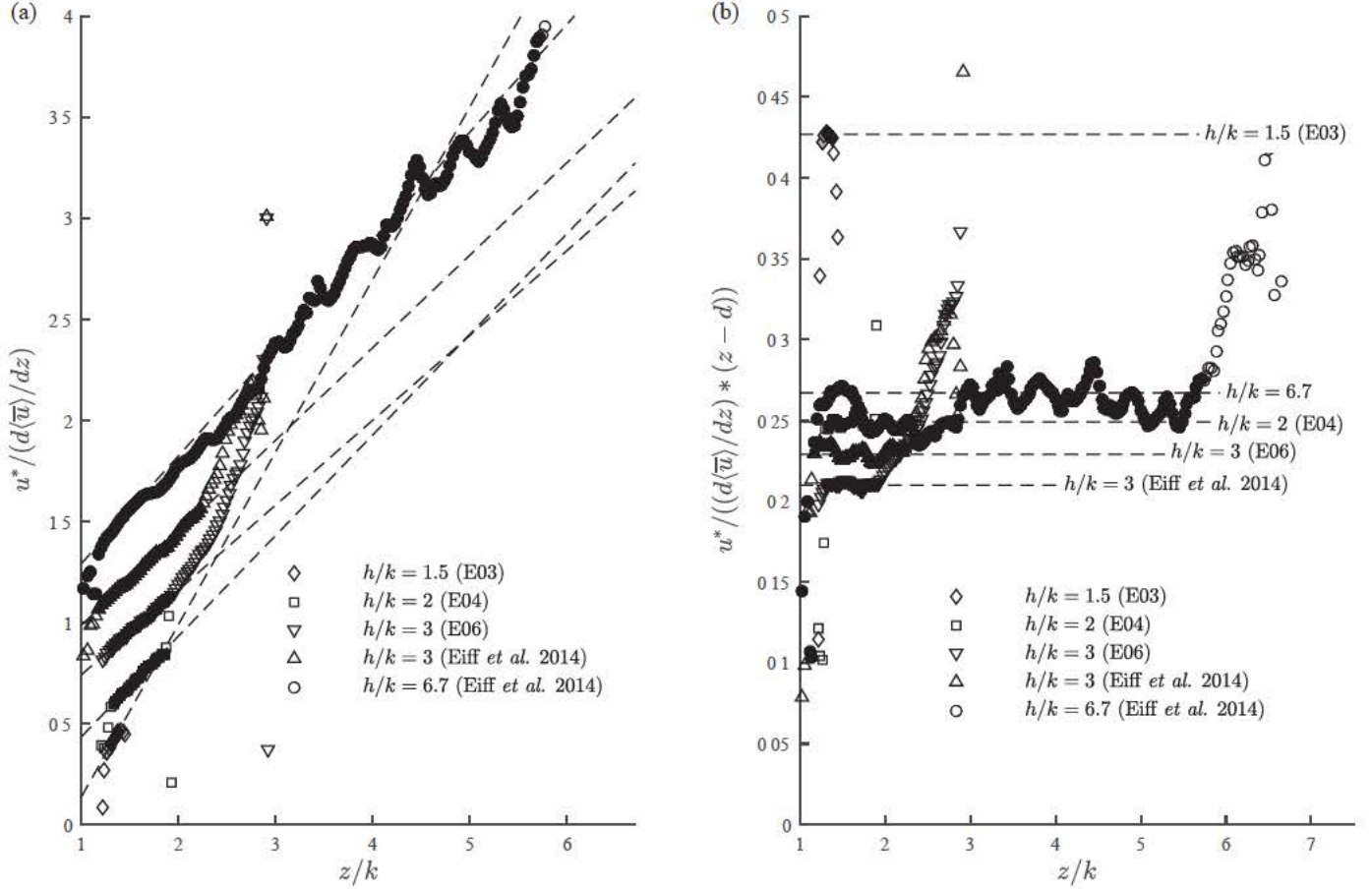
Figure 15   Evaluation of $\kappa_{h/k}$ for all flow regimes using the indicator function based on the the work of Spalart (1988) and Mohajeri et al. (2015). Filled symbols indicate the validity range of the linear fit used in the method. (a) Estimation of $\kappa_{h/k}$ from the slope of $u_*/(d\langle\bar{u}\rangle/dz)$. Corresponding linear fits are plotted in dashed lines. For clarity, plots for the different flow regimes are translated vertically in the figure. (b) $\kappa_{h/k}$ (dashed lines) corresponding to the flat part of the inverse of the indicator function (Eq. (7))

Table 5   Logarithmic-law parameters with $\kappa_{h/k}$ estimated with the indicator function (free-κ approach), for all regimes investigated here and from experiments of Eiff et al. (2014)[a]

h/k	u_*/U_{max}	$\kappa_{h/k}$	d/k	k_s/k	k_s/h	Π	z_m/k	z_M/k	η_{max}	z_m^ϵ/k	z_M^ϵ/k	η_{max}^ϵ
6.7[a]	0.069	0.267 ± 0.002	0.455 ± 0.001	1.290 ± 0.001	0.193	0.00	2.86	4.26	0.61	2.51	6.31	0.94
3[a]	0.082	0.229 ± 0.002	0.484 ± 0.001	0.852 ± 0.001	0.284	0.00	1.31	2.23	0.69	1.06	2.48	0.77
3 (E06)	0.079	0.210 ± 0.002	0.426 ± 0.001	0.995 ± 0.001	0.332	0.00	1.29	1.91	0.57	1.17	2.14	0.67
2 (E04)	0.084	0.249 ± 0.004	0.629 ± 0.001	0.601 ± 0.001	0.301	0.00	1.31	1.90	0.93	1.28	1.92	0.94
1.5 (E03)	0.085	0.427 ± 0.007	0.840 ± 0.004	0.254 ± 0.001	0.169	0.04	1.24	1.40	0.93	1.21	1.47	0.96

The fitted logarithmic-law parameters are d, k_s, $\kappa_{h/k}$, and the lower and upper bounds z_m and z_M. $\eta_{max} = (z_M - d)/(h - d)$. z_m^ϵ and z_M^ϵ are the lower and upper bounds using a spatial convergence error estimate $\epsilon_{\langle\bar{u}\rangle}$ with 95% confidence. $\eta_{max}^\epsilon = (z_M^\epsilon - d)/(h - d)$. Π is Coles' wake parameter.

5.2   Free-κ approach

The free-κ approach was applied to the three $h/k = \{1.5, 2, 3\}$ regimes of the present study as well as for the data of the $h/k = \{3, 6.7\}$ regimes used in the constant-κ approach by Eiff et al. (2014). Fig. 15a shows $u_*/(d\langle\bar{u}\rangle/dz)$ as a function of z/k and the logarithmic fits used to determine $\kappa_{h/k}$. The filled symbols indicate the range of the validated linear fits. Figure 15b shows the inverse of the indicator function Eq. (7), $u_*/(d\langle\bar{u}\rangle/dz * (z - d))$, after determining k_s and d from the second fit. The data points reveal approximately flat regions in

agreement with the $\kappa_{h/k}$ values (dashed lines) determined via the fits in Fig. 15a. The corresponding double-averaged velocity profiles are plotted in Fig. 14b where it can be seen that in all cases the fitted logarithmic laws (dashed lines) match rather well the data points in the validated ranges (solid symbols). It can also be observed that the velocity defect is smaller than in the constant-κ approach, in particular for the higher submergence ratios $h/k = \{3, 6.7\}$.

Table 5 summarizes all parameters obtained with the free-κ approach: the van Kármán constant $\kappa_{h/k}$, the relative displacement height d/k, the relative equivalent sand roughness k_s/k, and

the lower and upper bounds z_m/k and z_M/k. Coles' wake parameter Π has also been computed as well as the extended bounds by considering 95% confidence intervals as before. It can be seen in Table 5 that $\kappa_{h/k}$ found with this approach is smaller than 0.41 reaching a minimum of 0.21 at $h/k = 3$. At $h/k = 1.5$, $\kappa_{h/k} = 0.385$, almost as high as the standard value, while at $h/k = 6.7$, $\kappa_{h/k} = 0.267$. This behaviour is in accordance with the trend suggested by Gaudio, Miglio, and Dey (2010) but with a minimum at a higher h/k ratio (≈ 7), on the basis of widely scattered data compiled from several studies. The range $[z_m/h, z_M/h]$ of the optimally fitted logarithmic law for $h/k = 1.5$ is the same in both approaches with an upper bound of $\eta^\epsilon_{\max} = 0.96$. For $h/k > 1.5$, however, the free-κ approach yields higher upper bounds than with the constant-κ approach, with extended ranges $[z_m/h^\epsilon, z_M/h^\epsilon]$ almost reaching the whole available water depth over the roughness elements. This is in accordance with values close to zero found for the Coles' wake parameter Π and the observation of the velocity profiles in Fig. 14b. Considering that the free-κ approach has an additional free parameter, it is not surprising to obtain an even wider range.

The k_s/k values found with the free-κ approach are only slightly larger than for the constant-κ approach. Yet, although a decrease of k_s/k with decreasing values of h/k is observed as for the constant-κ approach, k_s/h is not constant any more, yielding higher values in the middle h/k range. This reflects the trend of $\kappa_{h/k}$. Similarly, the normalized displacement height d/k found with this approach is less robust than with the constant-κ approach, increasing as h/k decreases.

5.3 *Beyond the streamwise velocity profiles*

In uniform flow conditions, the double-averaged Navier–Stokes equations (e.g. Nikora et al., 2007) simplify into a linear profile of the total shear stress tensor, reading $\tau = u_*^2(1 - (z - k)/(h - k))$ since u_* is given by τ at $z = k$. Adopting the mixing-length model $\tau = \ell_m^2|\mathrm{d}\bar{u}/\mathrm{d}z|(\mathrm{d}\bar{u}/\mathrm{d}z)$ to relate this shear stress formulation to the law of the wake for double-averaged velocity $\langle \bar{u} \rangle$, yields a theoretical profile for the mixing length of the form:

$$\frac{\ell_m(z)}{h-d} = \kappa \left[\overline{1 - \frac{z-k}{h-k}} \, \frac{h-d}{z-d} + \pi \Pi \sin\left(\pi\frac{z-d}{h-d}\right) \right]^{-1}$$

(10)

This formulation is analogous to the mixing-length formulation for smooth uniform flows of Nezu and Rodi (1986), extended here to rough-wall turbulent boundary layers containing the logarithmic-law and Coles' law of wake.

Mixing lengths calculated from the experimental profiles of τ and $\mathrm{d}\langle\bar{u}\rangle/\mathrm{d}z$ are plotted in Fig. 16 for the flow regimes studied here and for the experiments of Eiff et al. (2014) for $h/k = 3$ and $h/k = 6.7$. Predictions of Eq. (10) for the approach with $\kappa = 0.41$ and the free-κ approach (via $\kappa = \kappa_{h/k}$ and the displacement height d) are also plotted in the same figure.
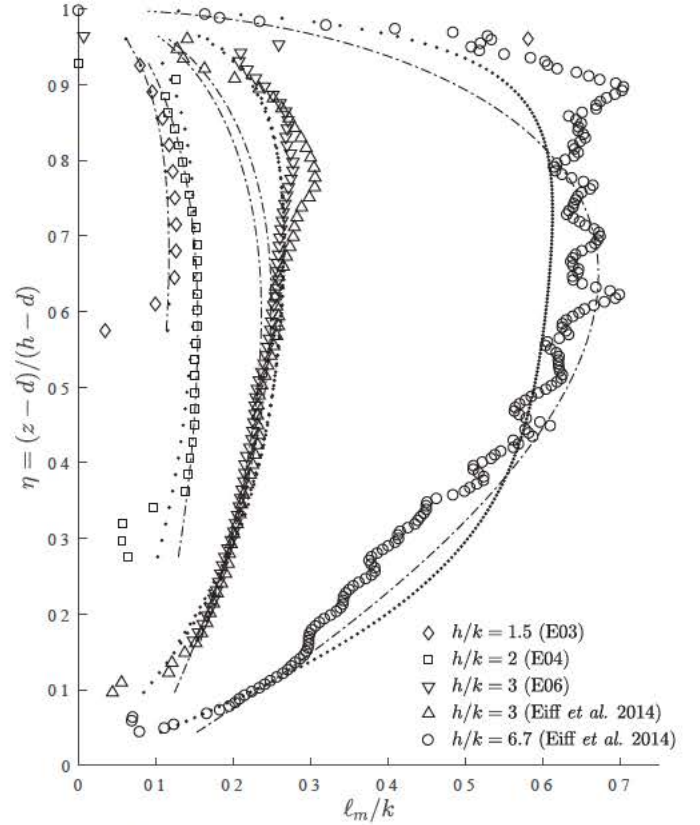

Figure 16   Mixing length ℓ_m/k and prediction given by Eq. (10) using the displacement height d from the $\kappa = 0.41$ fitting approach ($\cdots$) and the free-κ fitting approach ($\cdot - \cdot -$)

It can be observed in Fig. 16 that the values of κ and d found with both approaches allow Eq. (10) to capture the experimental profiles on a large portion of the water depth. The free-κ approach, however, appears to be better towards the free surface, while the constant-κ approach is also able to capture the behaviour near the rough bed, i.e. for $z \to k$, where the free-κ approach faces difficulties. These observations are in accordance with the extended fitting ranges $[z_m^\epsilon, z_M^\epsilon]$ which for $h/k > 1.5$ extend higher towards the free surface with the free-κ approach than with the constant $\kappa = 0.41$ approach, the latter, however, being more efficient near the roughness elements.

In Fig. 17a and 17b, profiles of the streamwise and vertical spatially-averaged normal stresses are plotted with the fitting laws proposed by Kironoto and Graf (1994) and Nezu and Rodi (1986), using the external variable $\eta = (z - d)/(h - d)$ which depends on the logarithmic-law fitting approach. Figure 17a shows the results for the constant-κ approach and Fig. 17b for the free-κ one. Data from the experiments of Eiff et al. (2014) for $h/k = 3$ and $h/k = 6.7$ are included in the figures. Comparing both figures, it can be observed that the collapse of the profiles is better with the $\kappa = 0.41$ approach (Fig. 17a) than with the free-κ approach (Fig. 17b), in particular in the lower part of the flow ($\eta < 0.5$). Moreover, the experimental profiles with $\kappa = 0.41$ are in better accordance with the fitting laws of Kironoto and Graf (1994) (rough open-channel
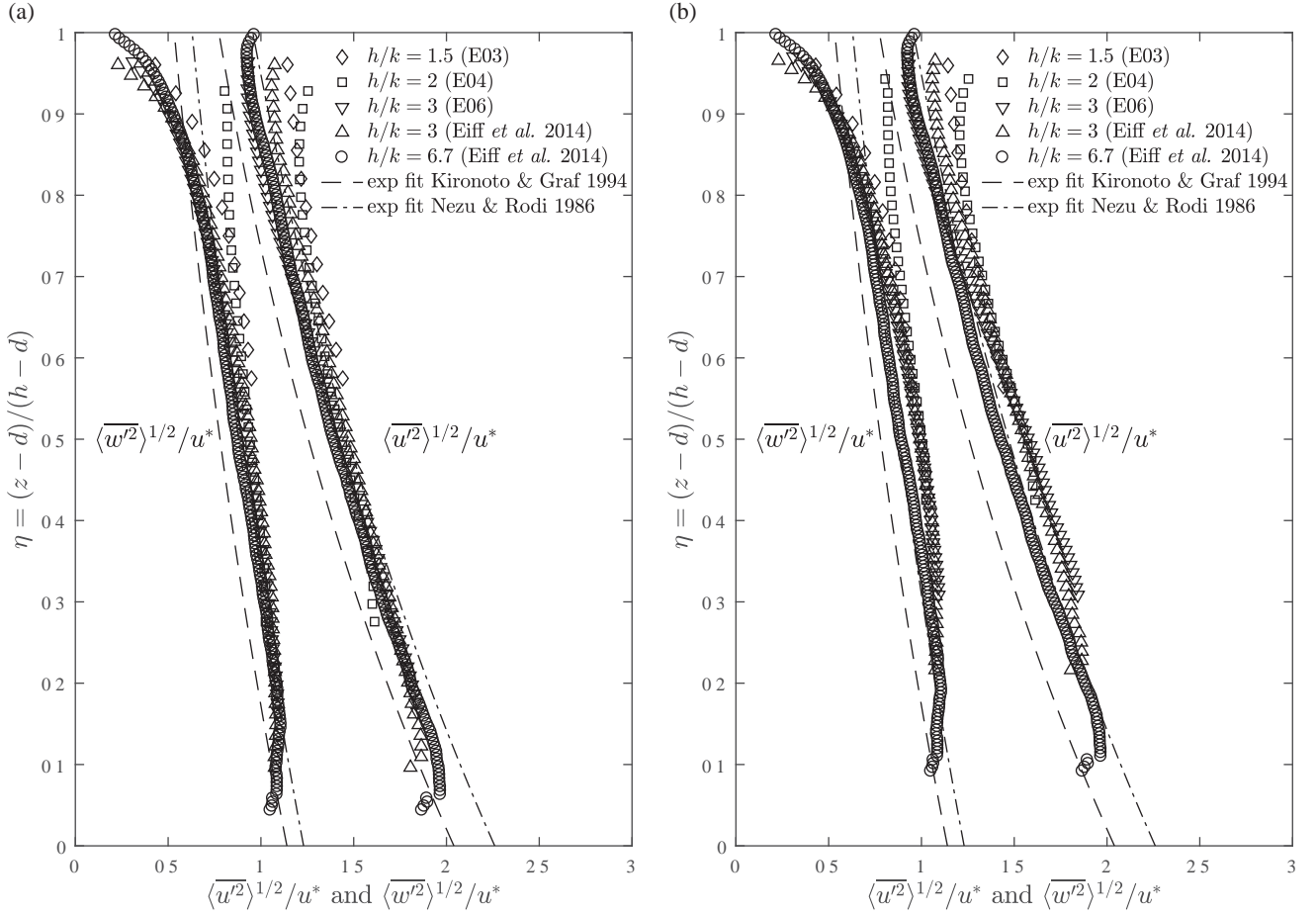
Figure 17 Normalized spatially-averaged normal stresses $\langle \overline{u'^2} \rangle / u_*$ and $\langle \overline{w'^2} \rangle / u_*$. η computed with displacement height d obtained from (a) the constant-κ approach and (b) the free-κ approach. The exponentially fitted profiles of Kironoto and Graf (1994) and Nezu and Rodi (1986) are also given for comparison

flows with $6 < h/k < 20$) and Nezu and Rodi (1986) (smooth and rough high-submergence open-channel flows). The relatively good consistency of the results for all submergence ratios and agreement within the scatter of existing data with high submergence ratios suggests a universal behaviour. This universality is better captured with the constant-κ approach (through the estimation of the displacement height d). It should be noted that the difference in the outer layer between the two equivalent $h/k = 3$ regimes but with different Froude numbers suggests the presence of small surface-wave induced effects. These are likely also the cause for the deviations for the low submergence regimes $h/k = 2$ and $h/k = 1.5$ for $\eta > 0.6$. Regime $h/k = 2$ in particular shows signs of the resonant waves with an upward curvature in both components as $z \to \eta = 1$.

Amir and Castro (2011) concluded that for developing zero-pressure-gradient boundary layers down to $\delta/k = 6$, outer-layer similarity of the Reynolds stresses is found. They based this on the observation that the anisotropy ratio $\langle \overline{w'^2} \rangle / \langle \overline{u'^2} \rangle$ was unaffected down to this δ/k ratio. Figure 18a shows this anisotropy ratio in the present regimes as well as for $h/k = \{3, 6.7\}$ from Eiff et al. (2014) along with predictions inferred from the available exponential fits of Kironoto and Graf (1994) and Nezu

and Rodi (1986). Here, the displacement height d based on the $\kappa = 0.41$ approach has been used. The general collapse is rather good across the entire depth, except again near the free surface for the resonant-wave influenced regime $h/k = 2$. In the lower part of the flow (i.e. $\eta < 0.5$), this ratio slightly increases from 0.3 to 0.4, as expected from the empirical laws of Kironoto and Graf (1994), which predict an almost linear increase of the turbulence anisotropy ratio from 0.3 to 0.5 in the range $\eta \in [0, 1]$. Even the lowest submergence regimes $h/k = 1.5$ and $h/k = 2$ exhibit the same level of anisotropy in the lower part of the flow for $\eta < 0.7$ of about 0.4, showing that there, large turbulent eddies exhibit a similar structure for all h/k examined. This similarity even extends to the zero-pressure-gradient smooth and rough boundary layers examined by Amir and Castro (2011) who also found a ratio of about 0.4 down to $\delta/k = 6$ ratios at mid-height.

Figure 18b shows the anisotropy ratio of the lateral to the longitudinal stresses, $\langle \overline{v'^2} \rangle / \langle \overline{u'^2} \rangle$, for the three available regimes, $h/k = \{1.5, 2, 3\}$. This anisotropy ratio is clearly affected by the relative submergence. As h/k decreases, the ratio increases, indicating an increased transfer of turbulent energy to lateral motions as the water-depth decreases. This is consistent
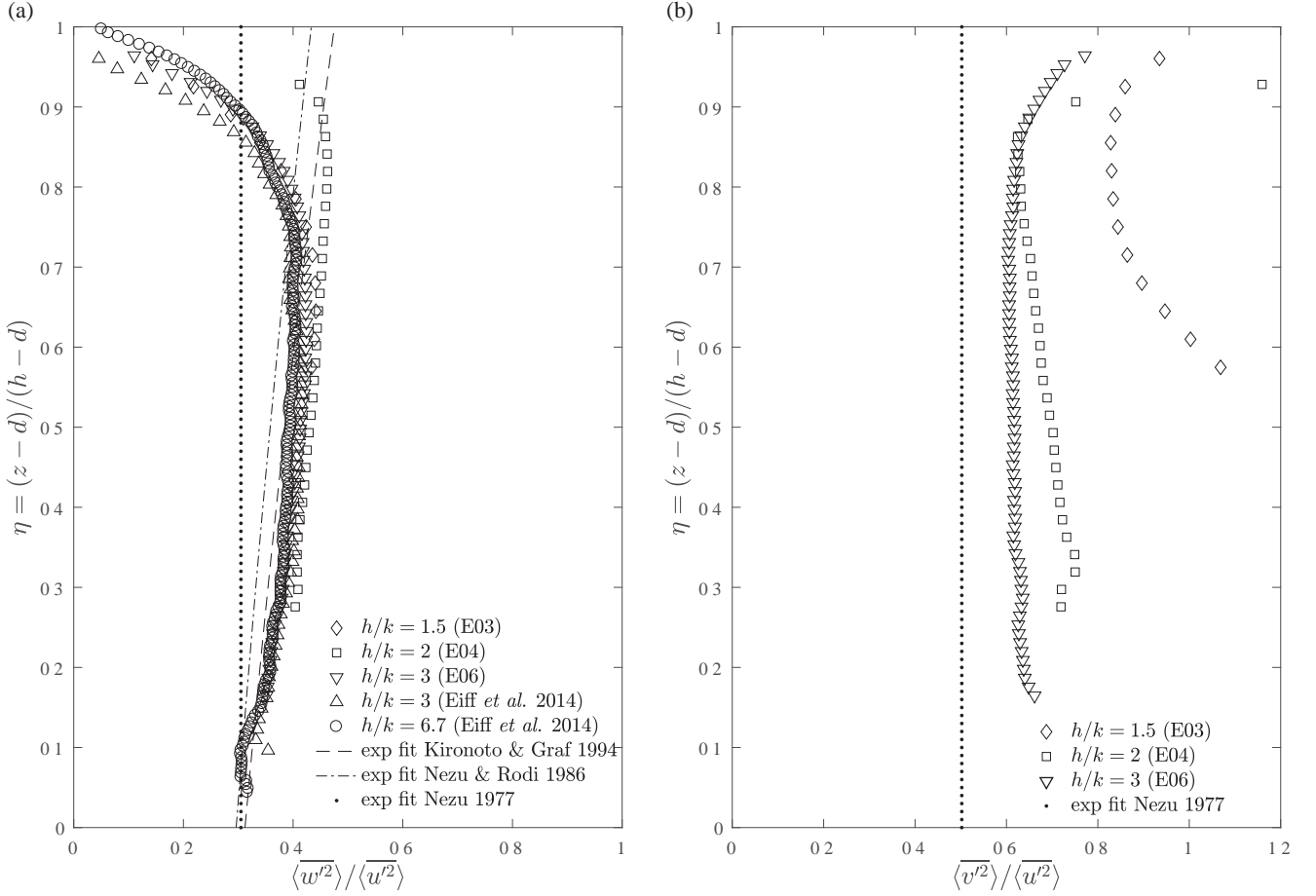
Figure 18   Turbulence anisotropy ratios, (a) $\langle\overline{w'^2}\rangle/\langle\overline{u'^2}\rangle$ and (b) $\langle\overline{v'^2}\rangle/\langle\overline{u'^2}\rangle$, as a function of $\eta = (z - d)/(h - d)$ (where d is the displacement height estimated with the constant $\kappa = 0.41$ method), along with predictions inferred from available exponential fits of Kironoto and Graf (1994), Nezu and Rodi (1986) and Nezu (1977)

with the increasingly strong inter-plane lateral shear on the roughness-pattern scale and the increased spatially-averaged lateral normal stress observed earlier. Unfortunately, the data of Eiff et al. (2014) are not stereoscopic so no higher submergence ratios are available to examine at which relative submergence this anisotropy ratio becomes universal, perhaps as low as 3. The exponential fits given by Nezu (1977) (also cited in Nezu & Nakagawa, 1993) give a constant $\langle\overline{v'^2}\rangle/\langle\overline{u'^2}\rangle = 0.5$ which is lower than the central value of about 0.6 found here with $h/k = 3$. However, the scatter of the data underlying these fits is quiet large. The exponential fits of Nezu (1977) also underestimate the vertical to longitudinal normal stress ratio, as seen in Fig. 18a.

6   Conclusion

The effect of low relative submergence ratios $h/k = \{1.5, 2, 3\}$ on the turbulent features of an open-channel flow over a rough homogeneous bed was investigated via stereo-PIV measurements in several planes for each submergence ratio in order to obtain well-converged double-averaged statistics.

Examination of the mean flow fields revealed mean secondary flows at the roughness scale. These secondary flows are significantly modified as the relative submergence ratio h/k decreases. In the lowest relative submergence ratio case examined, $h/k = 1.5$, a mean counter-rotating vortex in the lateral (y, z)-plane over the roughness pattern with a typical length scale of the same order of magnitude as the effective water depth $(h - d)$ can be inferred. Those mean secondary flows have their main direction in the streamwise direction and appear centred over the roughness pattern. The counter-rotating vortex can be explained by a rigid wall assumption, where the free surface acts as a rigid wall. Then, the flow cannot adapt through a variation of the pressure gradient via free-surface oscillations and is forced to accelerate. As a consequence, the streamwise velocity component increases (as observed) and is distributed into the lateral and vertical directions. In particular, a jet-like flow in the alley between the cubes forms and the horizontal shear within the roughness pattern scale increases drastically, generating a recirculation in the lateral plane. The increasing horizontal shear as the relative submergence decreases generates higher lateral turbulence levels as seen in the spatially-averaged lateral normal stress profiles. It is also the cause of the strong non-universal isotropy of $\langle\overline{v'^2}\rangle/\langle\overline{u'^2}\rangle$, at least for $h/k \in [1.5, 2]$. The $\langle\overline{w'^2}\rangle/\langle\overline{u'^2}\rangle$

anisotropy, however, remains unaffected, revealing universal behaviour and values as in high relative-submergence open-channel flows or developing zero-pressure-gradient boundary layers.

In the intermediate low submergence regime, $h/k = 2$, resonant surface-gravity waves were triggered and clearly influenced the time-averaged vertical flow structure. For this specific case, modelling of the resonant wave was attempted in order to assess and remove it. The waves were identified as stationary, dispersive and almost two-dimensional deep-water surface gravity waves. A classical model using linear theory under the deep-water assumption was therefore applied which proved capable to quantitatively describe the resonant waves. This allowed the mean waves to be removed and to examine the turbulent flow structure. The study showed that both mean flow velocities and the theoretical resonance velocity on the one hand and the length-scale of the roughness pattern and water-depth on the other hand were close, explaining the trigger of the resonant waves. These waves are therefore Froude-number dependent and not a general feature of this submergence regime.

The roughness sublayer heights were assessed for each relative submergence ratio h/k based on the normalized spatial standard deviation $2D_s$ of all first and second-order statistics, following the method of Florens et al. (2013). While for $h/k = 6.7$ (Florens et al., 2013), the roughness sublayer height extends up to about 20% of the effective water depth $(h - d)$, it extends 30% for $h/k = 3$, 50% for $h/k = 2$, and 100% for the lowest investigated submergence ratio, $h/k = 1.5$. Thus, for $h/k = 1.5$, the roughness sublayer spans the entire water column.

It the classical view (e.g. Jiménez, 2004; Nikora et al., 2001), the logarithmic law exists above the roughness-sublayer but Amir and Castro (2011) and Eiff et al. (2014) show that it can penetrate the roughness sublayer. Here, the classical assumption was not made. The existence, bounds and parameters of the logarithmic law were investigated by two approaches, first, by assuming κ to be constant ($= 0.41$) and second, by an indicator-function method, initially proposed by Spalart (1988) for smooth walls, which determines κ. For all three submergence ratios, including $h/k = 1.5$, a logarithmic law was found with both approaches. The upper bound varies between both methods and almost reaches the free surface at the lowest submergence, $h/k = 1.5$. At h/k above 1.5 and as high as 6.7 (data of Eiff et al., 2014), the free-κ approach yields significantly higher upper-bounds than the constant-κ approach does. Examination of Coles' wake parameter (Π) shows that it is negligible with the free-κ approach, in accordance with the extended logarithmic range, while the constant-κ approach yields non-zero wake parameter values and with upper-bounds in agreement with the classical values at relatively high submergence $h/k = 6.7$ ($\eta = 0.15$). Analysis of a proposed rough-wall mixing-length model suggests that while the free-κ approach gives a better fit for the experimental data in the upper part of the flow, the constant-κ approach gives a better match near the top of the roughness elements. One can conclude that both approaches give consistent results, but the constant-κ approach is in better agreement with the mixing-length model and upper bounds of the logarithmic law.

The constant-κ method yields essentially constant relative displacement heights d/k. The equivalent sand roughness normalized by the water depth, k_s/h, is also approximately constant which would suggest d-type behaviour at first glance. However, $k_s/(h - d)$ increases significantly with decreasing h/k, i.e. k_s does not scale with the effective water depth $h - d$, which is the more pertinent boundary-layer depth scale. Indeed, in most studies, the origin of the coordinate system is taken at $z = d$ (after fitting the logarithmic law or using the centroidal approach of Jackson, 1981), so that the effective water depth $h - d$ is the water depth used. Since d scales with k, the difference between these two water thicknesses, h and $h - d$, becomes important for low values of h/k, as in the present study. The usual explanation for d-type behaviour in classical boundary layers with large δ/k or h/k is that when the streamwise separation between the roughness elements is relatively close with strong sheltering, vortex shedding from the roughness into the flow above is negligible and therefore isolates the upper flow from the roughness (Perry, Schofield, & Joubert, 1969). Such a view is held firmly only for two-dimensional obstacles such as transverse ribs or bars. In the three-dimensional roughness configuration of the present study, vortex shedding can still occur on the lateral sides, through the alleys, so that d-type behaviour is not expected, if it can be expected at all. On the other hand, d-type like behaviour with essentially constant $k_s/(h - d)$ was found for a staggered configuration of cubes with higher density ($\lambda_f = 0.4$) in Eiff et al. (2014), albeit the lowest h/k ratio investigated was only 3. For this staggered configuration with a high value of λ_f, little momentum exchange is possible between the troughs in the canopy, leading to the possibility of cavity flows in analogy with two-dimensional obstacles with strong sheltering and a d-type behaviour.

With the constant-κ approach, the extent of the logarithmic law, while small in terms of roughness heights, spans 15%, 31%, 54% and 96% of the effective water depth above the zero-plane displacement for $h/k = \{6.7, 3, 2, 1.5\}$, respectively. The law is found even though the scale separation h/k is as low as 1.5 and the roughness sublayer, with a threshold of 5%, extends throughout the water column. In other words, the logarithmic law is completely within the roughness sublayer. However, the more pertinent roughness scale is the equivalent sand roughness, k_s. While k_s/k is of order one at $h/k = 6.7$, for the lowest submergence ratio investigated here ($h/k = 1.5$), $k_s/k = 0.27$ (Table 4), so that $h/k_s = 6$. This is not far from the conservative estimate by Castro et al. (2013), $h/k_s \approx 9$, for the lower limit for outer-layer similarity in the case of zero-pressure gradient boundary layers.

Similarity with highly submerged boundary layers is indeed observed in the second-order statistics of the longitudinal and vertical velocity components. Yet, the variation of the outer-layer parameter Π with h/k in the constant-κ method or of

$\kappa_{h/k}$ in the free-κ method, as well as the associated change of the relative height of the logarithmic layer in both methods, implies that the outer mean flow is not self-similar with respect to the submergence ratio. While self-similarity is also observed in the $\langle \overline{w'^2} \rangle / \langle \overline{u'^2} \rangle$ profile, it is not in the $\langle \overline{v'^2} \rangle / \langle \overline{u'^2} \rangle$ profile which depends strongly on the submergence ratio h/k, at least in the range $h/k \in [1.5, 2]$ where it is driven by the roughness pattern's geometry.

In summary, in uniform open-channels where the bed roughness becomes a macro roughness relative to the flow depth, it has been shown that the logarithmic and wake-defect laws can still describe the velocity profile and roughness parameters to determine the bed friction for h/k as low as 1.5, while the classical second-order statistics of the longitudinal and vertical velocity components still follow the universal boundary-layer behaviour. Yet, at $h/k = 1.5$ the spatial standard deviation is non-negligible almost up to the free surface which requires that open-channel or *in situ* flow measurements should be performed accordingly. In particular, for point measurement techniques, acquisition times and the density of the number of samples at a fixed elevation must be high enough to yield reliable estimates of the double-averaged quantities, before any analysis. This was aided in the present study with a well-defined periodic pattern.

The observed persistence of the logarithmic law for very low submergence ratios suggests that friction factor formulations based on the logarithmic law are still relevant in these regimes. The total stress measurements showed that the friction velocity u_* at the canopy top is increasing as the relative submergence decreases. The total bed shear stress or resistive stress can be evaluated ($\tau_0 = \rho u_*^2 (1 + \Phi k / h)$, see Pokrajac et al. (2006) and Section 3.3), but to determine friction factors based on the vertically integrated or bulk velocity, the flow in the interstices also needs be known since its contribution to the flow rate increases with decreasing h/k. Florens et al. (2013) measured the interstitial flow for $h/k = 3$ and in future work, the use of transparent cubes will allow spatially converged measurements within the interstices for the complete range of h/k. Also, the results need to be extended to different roughness densities A_f over the full h/k range and to the irregular roughness of gravel beds to verify if the observed trends and observations have a more universal character.

Notation

A_f	=	frontal area of the periodic roughness pattern (m)
A_p	=	planar area of the periodic roughness pattern (m)
A_w	=	wave amplitude (m)
B_r	=	constant of the logarithmic law for rough beds (–)
d	=	displacement height (m)
D_s	=	non-dimensional spatial standard deviation coefficient (–)
D_{84}	=	84th percentile of grain size distribution (m)
Fr	=	Froude number (–)
g	=	gravitational acceleration (m s^{-2})
h	=	water depth (m)
h_n	=	normal water depth (m)
h_{rs}	=	top of the roughness sublayer (m)
k	=	roughness height (m)
k_s	=	equivalent-sand-roughness scale (m)
k_s^+	=	equivalent-sand-roughness Reynolds number (–)
k_w	=	wavenumber (m^{-1})
ℓ_m	=	mixing length (m)
L	=	roughness pattern length (m)
Q	=	water discharge (m^3 s^{-1})
R_h	=	hydraulic radius (m)
u	=	streamwise component of the velocity (m s^{-1})
U_d	=	free-stream bulk velocity (m s^{-1})
U_r	=	velocity for wave resonance (m s^{-1})
u_*	=	friction velocity at top of roughness elements (m s^{-1})
v	=	lateral component of the velocity (m s^{-1})
w	=	vertical component of the velocity (m s^{-1})
W	=	wake function (m s^{-1})
x	=	streamwise coordinate (m)
x_M	=	streamwise position of the measurement area in the flume (m)
x_0	=	streamwise origin for resonant waves (m)
y	=	lateral coordinate (m)
z	=	vertical coordinate (m)
z_0	=	roughness length (m)
z_0^+	=	roughness-length Reynolds number (–)
z_{fs}	=	free-surface z-location
z_m	=	lower bound of the linear regression for the logarithmic law (m)
z_m^ϵ	=	extended lower bound of the linear regression for the logarithmic law (m)
z_M	=	upper bound of the linear regression for the logarithmic law (m)
z_M^ϵ	=	extended upper bound of the linear regression for the logarithmic law (m)
β	=	camera angle ($^\circ$)
δ	=	boundary-layer thickness (m)

δ^+	=	boundary-layer thickness Reynolds number (–)
ΔU^+	=	roughness function (–)
Δ_x	=	streamwise grid step for PIV (m)
Δ_z	=	vertical grid step for PIV (m)
$\epsilon_{\langle\bar\phi\rangle}$	=	spatial convergence error with 95% confidence for the double-averaged quantity $\langle\bar\phi\rangle$ (–)
η	=	external variable (–)
$\eta_{\max}$	=	relative height of the upper bound for the logarithmic law (–)
$\eta_{\max}^\epsilon$	=	relative height of the extended upper bound for the logarithmic law (–)
κ	=	von Kármán constant (–)
$\kappa_{h/k}$	=	von Kármán constant found with the indicator function (–)
λ_f	=	frontal density (–)
ω	=	wave frequency (s^{-1})
Φ	=	canopy porosity (–)
Π	=	Coles' wake parameter (–)
τ_0	=	bed shear stress ($\mathrm{N\,m}^{-2}$)
τ_{ij}	=	total shear stress tensor ($\mathrm{N\,m}^{-2}$)
τ_k	=	shear stress at $z=k$ equal to ρu_*^2 ($\mathrm{N\,m}^{-2}$)
$\overline{\cdots}$	=	time-averaging operator
$\langle\cdots\rangle_x$	=	single-plane spatial-averaging operator (in x-direction)
$\langle\cdots\rangle$	=	spatial-averaging operator (in both y- and x-directions)
$\cdots'$	=	turbulent fluctuation component
$\tilde{\cdots}$	=	dispersive component

ORCID

Maxime Rouzes http://orcid.org/0000-0002-3329-7790
Frédéric Yann Moulin http://orcid.org/0000-0003-4682-7348
Olivier Eiff https://orcid.org/0000-0002-6451-6378

References

Al Faruque, M. A. A., & Balachandar, R. (2011). Seepage effects on turbulence characteristics in an open channel flow. *Canadian Journal of Civil Engineering, 38*(7), 785–799.

Alfredsson, P. H., Segalini, A., & Örlü, R. (2011). A new scaling for the streamwise turbulence intensity in wall-bounded turbulent flows and what it tells us about the "outer" peak. *Physics of Fluids, 23*(4), 041702.

Amir, M., & Castro, I. P. (2011). Turbulence in rough-wall boundary layers: Universality issues. *Experiments in Fluids, 51*(2), 313–326.

Bathurst, J. C. (1985). Flow resistance estimation in mountain rivers. *Journal of Hydraulic Engineering, 111*(4), 625–643.

Bayazit, M. (1976). Free surface flow in a channel of large relative roughness. *Journal of Hydraulic Research, 14*(2), 115–126.

Calluaud, D., & David, L. (2004). Stereoscopic particle image velocimetry measurements of the flow around a surface-mounted block. *Experiments in Fluids, 36*(1), 53–61.

Castro, I. P. (2007). Rough-wall boundary layers: Mean flow universality. *Journal of Fluid Mechanics, 585*, 469–485.

Castro, I. P., Segalini, A., & Alfredsson, P. H. (2013). Outer-layer turbulence intensities in smooth- and rough-wall boundary layers. *Journal of Fluid Mechanics, 727*, 119–131.

Coceal, O., Thomas, T. G., Castro, I. P., & Belcher, S. E. (2006). Mean flow and turbulence statistics over groups of urban-like cubical obstacles. *Boundary-Layer Meteorology, 121*(3), 491–519.

Cooper, J. R., Aberle, J., Koll, K., & Tait, S. J. (2013). Influence of relative submergence on spatial variance and form-induced stress of gravel-bed flows. *Water Resources Research, 49*(9), 5765–5777.

Eiff, O., Florens, E., & Moulin, F. Y. (2014). Roughness parameters in shallow open-channel flows. In A. J. Schleiss, G. De Cesare, M. Franca, & M. Pfister (Eds.), *River Flow 2014. Proceedings of the international conference on fluvial hydraulics* (pp. 287–292). Laussane, Switzerland.

Ferguson, R. (2007). Flow resistance equations for gravel- and boulder-bed streams. *Water Resources Research, 43*, W05427.

Flack, K. A., & Schultz, M. P. (2014). Roughness effects on wall-bounded turbulent flows. *Physics of Fluids, 26*(10), 101305.

Flack, K. A., Schultz, M. P., & Connelly, J. S. (2007). Examination of a critical roughness height for outer layer similarity. *Physics of Fluids, 19*(9), 095104.

Flack, K. A., Schultz, M. P., & Shapiro, T. A. (2005). Experimental support for Townsend's Reynolds number similarity hypothesis on rough walls. *Physics of Fluids, 17*(3), 035102.

Florens, E. (2010). *Couche limite turbulente dans les écoulements à surface libre: étude expérimentale d'effets de macro-rugosités* [Turbulent boundary layer in open-channel flows: An experimental study of macro-roughness influence] (Doctoral dissertation). Université de Toulouse, France. Retrieved from http://thesesups.ups-tlse.fr/1285/.

Florens, E., Eiff, O., & Moulin, F. (2013). Defining the roughness sublayer and its turbulence statistics. *Experiments in Fluids, 54*(4), 1500.

Franca, M. J., Ferreira, R. M. L., & Lemmin, U. (2008). Parameterization of the logarithmic layer of double-averaged streamwise velocity profiles in gravel-bed river flows. *Advances in Water Resources, 31*(6), 915–925.

Gaudio, R., Miglio, A., & Dey, S. (2010). Non-universality of von Kármán's κ in fluvial streams. *Journal of Hydraulic Research, 48*(5), 658–663.

Hanmaiahgari, P. R., Roussinova, V., & Balachandar, R. (2017). Turbulence characteristics of flow in an open channel with temporally varying mobile bedforms. *Journal of Hydrology and Hydromechanics, 65*(1), 35–48.

Hey, R. D. (1979). Flow resistance in gravel-bed rivers. *Journal of the Hydraulics Division, 105*(4), 365–379.

Jackson, P. S. (1981). On the displacement height in the logarithmic velocity profile. *Journal of Fluid Mechanics, 111*, 15–25.

Jiménez, J. (2004). Turbulent flows over rough walls. *Annual Review of Fluid Mechanics, 36*, 173–196.

Katul, G., Wiberg, P., Albertson, J., & Hornberger, G. (2002). A mixing layer theory for flow resistance in shallow streams. *Water Resources Research, 38*(11), 1250.

Keulegan, G. H. (1938). Laws of turbulent flow in open channels. *Journal of Research of the National Bureau of Standards, 21*, 707–741. Research paper RP1151.

Kironoto, B. A., & Graf, W. H. (1994). Turbulence characteristics in rough non-uniform open-channel flow. *Proceedings of the Institution of Civil Engineers - Water Maritime and Energy, 112*(4), 336–348.

Koll, K. (2006, September). Parameterisation of the vertical velocity profile in the wall region over rough surfaces. In R. M. L. Ferreira, E. C. T. L. Alves, J. G. A. B. Leal, & A. H. Cardoso (Eds.), *River Flow 2006. Proceedings of the international conference on fluvial hydraulics* (Vol. 1, pp. 163–172). Lisbon: Taylor and Francis.

Lavoie, P., Avallone, G., De Gregorio, F., Romano, G. P., & Antonia, R. A. (2007). Spatial resolution of PIV for the measurement of turbulence. *Experiments in Fluids, 43*(1), 39–51.

Lighthill, J. (2001). *Waves in fluids*. Cambridge: Cambridge University Press.

Macdonald, R. W. (2000). Modelling the mean velocity profile in the urban canopy layer. *Boundary-Layer Meteorology, 97*(1), 25–45.

Manes, C., Pokrajac, D., & McEwan, I. (2007). Double-averaged open-channel flows with small relative submergence. *Journal of Hydraulic Engineering, 133*(8), 896–904.

Marusic, I., Monty, J. P., Hultmark, M., & Smits, A. J. (2013). On the logarithmic region in wall turbulence. *Journal of Fluid Mechanics, 716*, R3.

Mohajeri, S. H., Grizzi, S., Righetti, M., Romano, G. P., & Nikora, V. (2015). The structure of gravel-bed flow with intermediate submergence: A laboratory study. *Water Resources Research, 51*(11), 9232–9255.

Nagib, H. M., & Chauhan, K. A. (2008). Variations of von Kármán coefficient in canonical flows. *Physics of Fluids, 20*(10), 101518.

Nezu, I. (1977). *Turbulent structure in open-channel flows* [English translation of the Japanese doctoral dissertation of Iehisa Nezu] (Doctoral dissertation). Kyoto University, Kyoto, Japan.

Nezu, I., & Rodi, W. (1985). Experimental study on secondary currents in open-channel flow. *Proceedings of the 21st congress of IAHR, Melbourne, Australia* (Vol. 2, pp. 114–119).

Nezu, I., & Rodi, W. (1986). Open channel flow measurements with a laser doppler anenometer. *Journal of Hydraulic Engineering, 112*(5), 335–355.

Nezu, I., & Nakagawa, H. (1993). IAHR Monograph. *Turbulence in open-channel flow*. Rotterdam: Balkema Pub.

Nikora, V., Goring, D., McEwan, I., & Griffiths, G. (2001). Spatially averaged open-channel flow over rough bed. *Journal of Hydraulic Engineering, 127*(2), 123–133.

Nikora, V., Koll, K., McEwan, I., McLean, S., & Dittrich, A. (2004). Velocity distribution in the roughness layer of rough-bed flows. *Journal of Hydraulic Engineering, 130*(10), 1036–1042.

Nikora, V., Koll, K., McLean, S., Dittrich, A., & Aberle, J. (2002, September). Zero-plane displacement for rough-bed open-channel flows. In Y. Zech & D. Bousmar (Eds.), *Riverflow 2002. Proceedings of the international conference on fluvial hydraulics* (Vol. 1, pp. 83–91). Louvain-la-Neuve, Belgium: Swets & Zeitlinger.

Nikora, V., McEwan, I., McLean, S., Coleman, S., Pokrajac, D., & Walters, R. (2007). Double-averaging concept for rough-bed open-channel and overland flows: Theoretical background. *Journal of Hydraulic Engineering, 133*(8), 873–883.

Nikuradse, J. (1933). Strömungsgesetze in rauhen Rohren. *VDI-Forschungsheft 361*, Beilage zu "Forschung auf dem Gebiete des Ingenieurwesens", Ausgabe B Band 4, Juli/August 1933.

Nikuradse, J. (1950). *Laws of flow in rough pipes*. Washington: National Advisory Committee for Aeronautics, Technical Memorandum 1292. [Translation of Nikuradse (1933).].

Perry, A. E., Schofield, W. H., & Joubert, P. N. (1969). Rough wall turbulent boundary layers. *Journal of Fluid Mechanics, 37*, 383–413.

Pokrajac, D., Campbell, L. J., Nikora, V., Manes, C., & McEwan, I. (2007). Quadrant analysis of persistent spatial velocity perturbations over square-bar roughness. *Experiments in Fluids, 42*(3), 413–423.

Pokrajac, D., Finnigan, J. J., Manes, C., McEwan, I., & Nikora, V. (2006, June). On the definition of the shear velocity in rough bed open channel flows. In R. M. L. Ferreira, E. C. T. L. Alves, J. G. A. B. Leal, & A. H. Cardoso (Eds.), *River Flow 2006. Proceedings of the international conference on fluvial hydraulics* (Vol. 1, pp. 89–98). Lisbon: Taylor and Francis.

Prasad, A. K., & Jensen, K. (1995). Scheimpflug stereocamera for particle image velocimetry in liquid flows. *Applied optics, 34*(30), 7092–7099.

Raupach, M. R., Antonia, R. A., & Rajagopalan, S. (1991). Rough-wall turbulent boundary layers. *Applied Mechanics Reviews, 44*(1), 1–25.

Rickenmann, D., & Recking, A. (2011). Evaluation of flow resistance in gravel-bed rivers through a large field data set. *Water Resources Research, 47*(7), W07538.

Rouzes, M. (2015). Etude expérimentale de l'hydrodynamique d'un écoulement turbulent à surface libre sur fond rugueux

à faible submersion [Experimental investigation of rough open-channel flows in very shallow conditions] (Doctoral dissertation). Université de Toulouse, France. Retrieved from http://oatao.univ-toulouse.fr/14164/1/rouzes.pdf.

Segalini, A., Örlü, R., & Alfredsson, P. H. (2013). Uncertainty analysis of the von Kármán constant. *Experiments in Fluids*, *54*(2), 1460.

Spalart, P. R. (1988). Direct simulation of a turbulent boundary layer up to $R_\theta = 1410$. *Journal of Fluid Mechanics*, *187*, 61–98.

Squire, D. T., Morrill-Winter, C., Hutchins, N., Schultz, M. P., Klewicki, J. C., & Marusic, I. (2016). Comparison of turbulent boundary layers over smooth and rough surfaces up to high Reynolds numbers. *Journal of Fluid Mechanics*, *795*, 210–240.

Townsend, A. A. (1980). *The structure of turbulent shear flow*. Cambridge: Cambridge University Press.

Vinuesa, R., Schlatter, P., & Nagib, H. M. (2014). Role of data uncertainties in identifying the logarithmic region of turbulent boundary layers. *Experiments in Fluids*, *55*(6), 1751.